Title
HYDROGEN REDUCTION OF COBALT FERRITE

Author
Porter, J.R.

Publication Date
1979-06-01

LBL-9801 c.2
Preprint

Lawrence Berkeley Laboratory
UNIVERSITY OF CALIFORNIA

Materials & Molecular
Research Division

To be submitted for publication

HYDROGEN REDUCTION OF COBALT FERRITE

J. R. Porter and L. C. De Jonghe

June 1979

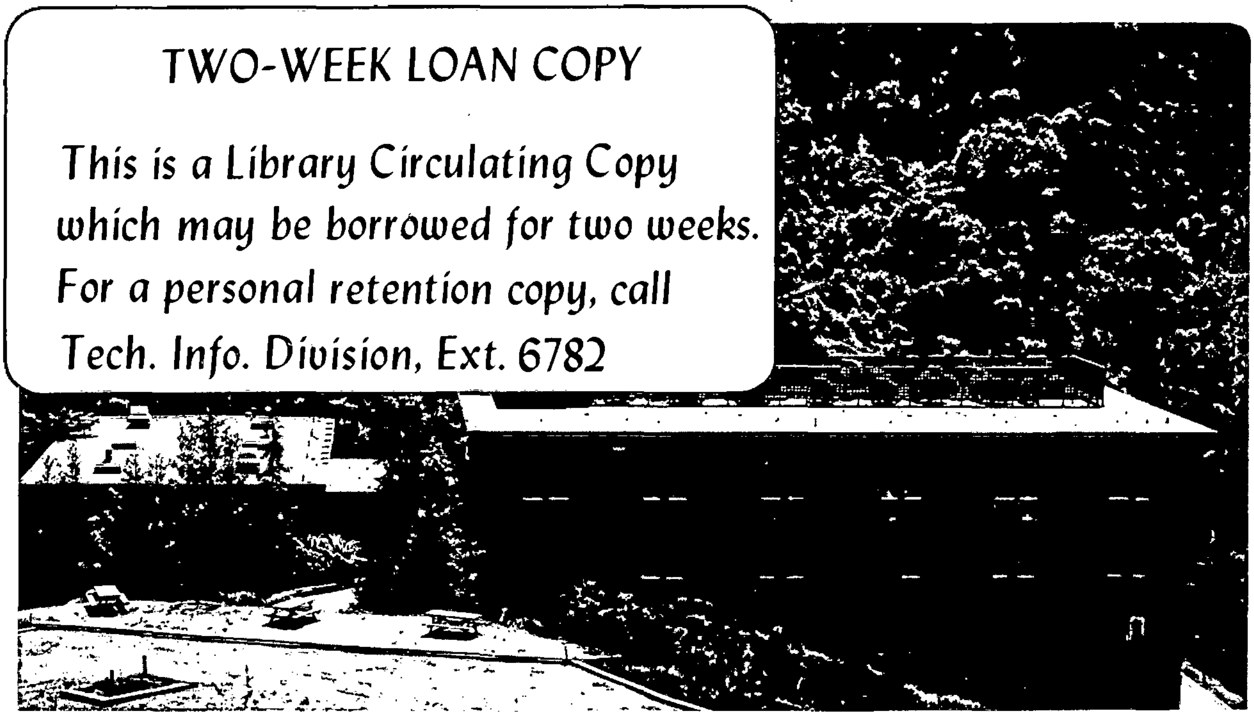

Prepared for the U.S. Department of Energy under Contract W-7405-ENG-48

HYDROGEN REDUCTION OF COBALT FERRITE

J. R. Porter
and
L. C. De Jonghe

June, 1979

Materials and Molecular Research Division
and
Department of Materials Science and Mineral Engineering
Lawrence Berkeley Laboratory
University of California
Berkeley, California 94720

ABSTRACT

The kinetics of reduction of cobalt ferrite by hydrogen as a function of reduction temperature and pressure have been measured by thermogravimetric analysis. A minimum in the rate as a function of temperature has been observed and its cause attributed to the formation of a cobalt wüstite subscale at higher reduction temperatures. A mathematical model, based on one derived by Spitzer, Manning, and Philbrook (1), has been used to interpret the results in terms of the rate constants for the individual steps in the reaction.

Optical microscopy has been used to characterize the morphology of the reduction product and, additionally, partially reduced single crystals of cobalt ferrite have been examined by transmission electron microscopy to characterize the microstructure of the reaction interface.

A fine network of pores in the reduced scale was shown to allow the reducing and product gases to reach the immediate vicinity of the chemical reaction. The scale of the porosity and consequently the effective gaseous diffusion coefficient in the scale were both shown to be functions of the reduction temperature and pressure. The chemical reaction rate constant was shown to follow Langmuir-Hinshelwood Kinetics and a model was developed to explain such kinetics by incorporating a solid-state diffusion step. Such a step was considered necessary to explain the development of the observed microstructures.

An incubation time for the development of a continuous cobalt-wüstite subscale at higher reduction temperatures was attributed to the different growth kinetics for the spinel-metal and spinel-wüstite interfaces.

Introduction

Rey and De Jonghe, in their study of the effect of aluminum doping on the reduction kinetics of cobalt ferrite, noticed that for both doped and undoped material, the reaction rate decreased with increasing reduction temperature over a certain temperature range (2). They reported that the temperature corresponding to the minimum rate was dependent on the level of aluminum doping and attributed the anomaly to the appearance of a wüstite-type subscale at high reduction temperatures.

A similar effect has been noticed for the reduction of iron oxides. Turkdogen and Vinters noticed that the reduction rate of hematite went through a minimum at around 570°C, which is the minimum temperature at which wüstite is thermodynamically stable (3). Quets, Wadsworth, and Lewis noticed the same effect for the reduction of magnetite and reported a much lower activation energy for reduction above the wüstite stability temperature than below it (4). A reaction rate minimum has also been reported for the reduction of cobalt oxide. Lilius observed that when cobalt oxide was reduced at low temperatures, the cobalt scale offered little resistance to gaseous diffusion, whereas at higher temperatures, the cobalt scale was less porous (5). In this case, the reaction rate decrease was attributed to the changes in the scale morphology at different reduction temperatures.

Mathematical models describing the kinetics of reduction reactions have been widely used to differentiate between the possible rate controlling steps which affect reduction rates. The model developed by Spitzer, Manning, and Phillbrook allowed for the possibility of three different phenomena to contribute to the resistance to reaction; namely, the mass transfer resistance of the reacting gases between the bulk gas stream and the specimen surface, the diffusion through the porous reduced metal scale and the chemical reaction itself (1). Although their model was developed to describe the reduction of spheres of oxide, a similar approach can be used to develop equations applicable to more than one specimen geometry. More recently, more sophisticated models have been developed which are applicable to different specimen geometries. Szekeley, Evans, and Sohn have developed a model which equates reduction parameters in a dimensionless form which can be applied to the reduction of spheres, cylinders, and slabs of both porous and non-porous solids (6).

However, as noted by Turkdogen and Vinters, no single rate equation accurately describes observed behavior over the whole range of reaction conditions encountered and for a full understanding of the reduction of any one oxide, further characterization of the individual steps of the reaction sequence is essential (3). For the example of cobalt ferrite reduction, further examination of the chemical reduction step is most likely to lead to an understanding of the reaction rate anomaly, since it appears to be associated with the development of a wüstite subscale. From the kinetic data and by using the rate equations, it is possible to calculate the apparent chemical reaction rate constants for the reaction for various temperatures and pressures. This information allows predictions to be made with regard to the possible rate controlling sub-steps of the chemical reaction step itself. For example, one of the simplest descriptions of a chemical reaction step, is that the reaction is first order and reversible. In such a case, the reaction rate constant is a function of temperature but not of reactant pressure, and the rate is described by an equation of the form:

$$J(0) = k_1 c_{H_2} - k_{-1} c_{H_2O} \qquad (1)$$

Such simple kinetic behavior is not always observed, however. The chemical reaction step for the reduction of several oxides has been reported to follow Langmuir-Hinshelwood kinetics. McKewan reported that the rate of reduction of magnetite below 570°C was proportional to hydrogen pressure up to one atmosphere, but approached a maximum rate at higher pressures (7). Langmuir-Hinshelwood kinetics can be described by an expression of the form

$$J(0) = \frac{a^* c_{H_2}}{1+b^* c_{H_2}} \qquad (2)$$

for the case of reduction by pure hydrogen (7). Langmuir-Hinshelwood kinetics have been attributed to reaction rates limited by adsorption and desorption (6, 7) and to reaction rates limited by solid-state diffusional processes (4). In the latter case, Quets, Wadsworth, and Lewis explained the kinetics of reduction of magnetite at temperatures above 570°C in terms of control by cation diffusion across a protective wüstite subscale.

The microstructural changes which occur in the vicinity of the reaction interface all contribute to the measured value of the chemical reaction rate constant. Swann and Tighe (8) and Porter and Swann (9) studied the microstructural changes associated with the reduction of hematite to magnetite and showed that solid state cation diffusion was necessary in the interface region. This short-range diffusion would then be an integral part of the chemical reaction step. While this development of scale microstructure is part of the chemical reaction, the microstructure itself determines the resistance to gaseous diffusion across the scale. The rate equation can be used to calculate effective diffusion coefficients, and these values can then be related to the scale microstructures.

In order to analyze the kinetic data, a simplified version of the Spitzer, Manning, and Philbrook model has been developed, which equates the scale growth rate to the kinetic parameters. The reaction sequence considered was:

1) External mass transfer of the reactant gas to the specimen surface.
2) Diffusion of the reactant gas through the porous shell layer.
3) The chemical reaction at the shell-core interface.
4) Outward diffusion of the product gas through the shell layer.
5) External mass transfer of the product gas.

In order to derive their equation, Spitzer, Manning, and Philbrook made the following assumptions:

1) The reduction was topochemical.
2) The unreduced oxide was fully dense.
3) The reaction was first order and reversible.

In the simplified version of the equation the following additional assumptions are made:

1) That the bulk gas is pure hydrogen.
2) That the mass transfer and effective diffusion coefficients are the same for the reactant and product gas.
3) That the reaction is irreversible ($K_e >> 1$).

With these assumptions, when considering the reduction of a slab, the following flux equations result for each step:

1) $$J\,(H_2) = -k_m\,(c_{H_2}^{b} - c_{H_2}^{o}) \qquad (3)$$

2) $$J\,(H_2) = \frac{-D_{H_2/H_2Oeff}}{\xi}\,(c_{H_2}^{o} - c_{H_2}^{i}) \qquad (4)$$

3) $$J\,(0) = k_r\,c_{H_2}^{i} \quad \frac{k_r}{K_e}\,c_{H_2O}^{i} \qquad (5)$$

4) $$J\,(H_2O) = \frac{D_{H_2/H_2Oeff}}{\xi}\,(c_{H_2O}^{i} - c_{H_2O}^{o}) \qquad (6)$$

5) $$J\,(H_2O) = k_m\,c_{H_2O}^{o} \qquad (7)$$

Now: $$J\,(H_2) = -J(0) = -J(H_2O) \qquad (8)$$

Equations 3-7 can be arranged as follows:

$$\frac{J(0)}{k_m} = c_{H_2} - c_{H_2}^{o} \qquad (9)$$

$$\frac{J(0)\xi}{D_{H_2/H_2Oeff}} = c_{H_2}^{o} - c_{H_2}^{i} \qquad (10)$$

$$\frac{J(0)}{k_r} = c_{H_2}^{i} - c_{H_2O}^{i} \qquad (11)$$

$$\frac{J(0)\xi}{D_{H_2/H_2Oeff}} \cdot \frac{1}{K_e} = \frac{c_{H_2O}^{i}}{k_e} - \frac{c_{H_2O}^{o}}{k_e} \qquad (12)$$

$$\frac{J(0)}{k_m} \cdot \frac{1}{K_e} = \frac{c_{H_2O}^{o}}{k_e} \qquad (13)$$

If equations 9-13 are added together and rearranged, the following rate equation results:

$$J(0) = c^b_{H_2}\left(\frac{1}{k_m(1+\frac{1}{K_e})} + \frac{\xi}{D_{H_2/H_2Oeff}\,(1+\frac{1}{K_e})} + \frac{1}{k_r}\right)^{-1} \qquad (14)$$

Now $c^b_{H_2} = \frac{p^b_{H_2}}{RT}$ (15)

and $J(0) = \xi\, c_0$ (16)

When $K_e >> 1$, equations 14-16 reduce to:

$$\dot{\xi} = \frac{p^b_{H_2}}{RTc_0}\left(\frac{1}{k_m} + \frac{\xi}{D_{H_2/H_2Oeff}} + \frac{1}{k_r}\right)^{-1} \qquad (17)$$

Equation 17 can be tested by converting the thermogravimetrically measured weight loss data to scale thickness data, using simple geometry and plotting the reciprocal of the reaction rate against the scale thickness. The intercept of the reciprocal rate, layer thickness plot will allow $(\frac{1}{k_m} + \frac{1}{k_r})$ to be obtained and the slope will give D_{H_2/H_2Oeff}.

Although the equation was derived assuming a first order reaction, the equation remains valid for non-first order reactions if k_r is considered to be a function of pressure. For example, a system following Langmuir-Hinshelwood kinetics, when analyzed using equation 17, would indicate a reaction rate constant with a pressure dependence of the form:

$$k_r = \frac{k'}{k'' + p_{H_2}} \qquad (18)$$

Plots of reciprocal reaction rate versus scale thickness have also been used by Olsson and McKewan in their study of the effective diffusion coefficient of H_2/H_2O in the scale of reduced iron oxides (10, 11).

Experimental Procedure

Thermogravimetric Analysis

The material used in the thermogravimetric analysis, T.G.A., experiments was dense, polycrystalline cobalt ferrite supplied by Countis Industries and had a grain size of about 20 μm. Specimens were cut from bars of this material and had dimensions 1 cm x 1 cm x 0.06 cm.

The thermogravimetric analysis apparatus, shown schematically in Figure 1, consisted of a vertical tube furnace in which the reduction gas passed from top to bottom. The specimens were suspended directly from a Cahn RG microbalance in a 1.9 cm hang-down tube and the weight of the specimen was recorded continuously. The pressure of the flowing hydrogen could be held constant to within 0.5 torr between 30 torr and 400 torr. The temperature in the immediate vicinity of the specimen was measured with a monitoring thermocouple.

Specimens were heated to the reduction temperature in about 0.2 torr of nitrogen during which time, no reduction took place. Once a steady temperature was reached, the flow of hydrogen was started and the reduction timed from this point. Depending on the reduction pressure, it took 30 to 60 seconds for the pressure to fully stabilize at the desired value, and there was a consequent loss of data during this time. After complete reduction, specimens were cooled in flowing hydrogen. It was found that a flow rate of hydrogen of 25 ml STP s^{-1}, was sufficient under all conditions used to prevent bulk hydrogen starvation.

The thermogravimetric experiments generated the instantaneous weight of the specimens as a function of time. Since the specimens were shown to reduce in a topochemical fashion, without measurable shrinkage, the weight loss kinetics determined by T.G.A. were converted to product layer growth kinetics. The relationship between the measured weight loss and the calculated layer thickness is given in Appendix 1.

Crystal Growth

Single crystals of cobalt ferrite, from which the specimens for transmission electron microscopy were prepared, were grown from a borax flux. The procedure adopted was based on the method of Galt, Matthias, and Remeika (12).

Preliminary experiments established that a good yield of cobalt ferrite single crystals could be obtained when 2.86 g cobalt carbonate, 3.84 g ferric oxide, 10.24 g borax and 0.17 g boric acid were used as starting materials. The mixture, placed in a platinum crucible with a tightly fitting, but not completely sealed, lid was held at 1330°C for 2 hours and cooled to 800°C at a controlled rate of 2°C per hour. The resulting crystals were leached from the flux using hot, dilute nitric acid. The crystals were faceted on {111} planes and the larger ones had dimensions of a few millimeters across.

Transmission Electron Microscopy

Specimens for electron microscopy were prepared in the following manner. The as-grown single crystals were cut into slices and mechanically ground until they were 50 μm thick. At this stage, the crystals were partially reduced for very short times at low hydrogen pressures in the thermogravimetric analysis apparatus and the reduction was stopped by dropping the specimen out of the hot zone with the hydrogen still flowing. The partially reduced specimens were then ion milled parallel to the reaction interface until the wedge-shaped electron transparent regions intersected the reaction interface.

Light Microscopy

Specimens for light microscopy were prepared using standard metallographic techniques and were etched in dilute hydrochloric acid to reveal the presence of any wüstite-type phase.

Results

1) Thermogravimetric Analysis Experiments

Figure 2 shows the kinetics of the metal product layer growth during reduction at 100 torr at four selected temperatures: 500°C, 600°C, 700°C, and 800°C. Since the specimens were initially all 0.6 mm thick, the reduction was complete for a shell layer thickness of 0.3 mm. Figure 2 clearly demonstrates the anomalous kinetics as a function of temperature. Between 500°C and 600°C the rate increased as the reduction temperature increased. When reduced at 700°C, there was an initial rapid rate, which was higher than the rate at 600°C, but after a certain layer thickness had built up, the rate dropped and the reaction proceeded more slowly. For reduction at 800°C, the initial rapid rate was not observed and although the rate was faster than during the later stages of reduction at 700°C, the rate was still slower than when reduced at 500°C.

Further data, from experiments conducted below the temperature of the rate anomaly, are shown as the inverse rate versus the product layer thickness in Figure 3. It can be seen that when the data are plotted in this way, they yield straight lines at reduction temperatures of 660°C and below. For reduction at 680°C, a very significant deviation from linearity is observed. This temperature corresponds to the onset of the rate anomaly.

The straight lines can be analyzed in terms of equation 17. In the derivation of equation 17, it was assumed that the exhaust gas remained essentially pure hydrogen. A calculation of the H_2/H_2O ratio of the exhaust gas for the fastest reduction rate encountered is given in Appendix 2, and the value was sufficiently high for the assumption to be considered valid. A calculation using established fluid mechanics expressions of the external mass transfer coefficients for reduction in 100 torr of hydrogen at 500°C, 600°C, 700°C, and 800°C is given in Appendix 3, and the values compared with the experimentally observed reaction rates.

For reduction at 500°C, the extrapolated reciprocal rate for zero layer thickness was 20709 $(\mathrm{cm\ s^{-1}})^{-1}$, which could be substituted into equation 17 to yield a value for $(k_r^{-1} + k_m^{-1})^{-1}$ of 2.1 cm s^{-1}. The calculated value for k_m was 179 cm s^{-1}, from which it can be established that $k_m \simeq 50\ k_r$ and so can be neglected. Similarly k_m can be neglected at 600°C and at 700°C and 800°C, the overall reaction rate is slower than at 600°C. Consequently, the combined reaction constant $(k_r^{-1} + k_m^{-1})^{-1}$, obtained from equation 17, is, in fact, simply the chemical rate constant k_r.

The effective binary diffusion coefficients of H_2/H_2O through the scale of the reaction product can be obtained from the slopes of the straight lines using equation 17. Values for k_r and $D_{H_2/H_2O\mathrm{eff}}$, for reduction experiments conducted at 100 torr, are listed in Table 1.

The reduction kinetics at 600°C as a function of the bulk hydrogen pressure are plotted in Figure 4. Figure 4a shows the extent of reaction as a function of time and Figure 4b the reciprocal reaction rate as a function of the extent of reaction. Note that the slopes decrease with increasing hydrogen pressures. Again values for k_r and

$D_{H_2/H_2O\,eff}$ were obtained and are presented in Table 2.

The two stages apparent in the reduction of specimens reduced at temperatures close to the rate minimum temperature in 100 torr of hydrogen are clearly shown in Figure 5. At 660°C, the reaction mechanism appeared to be the same as that operating at lower temperatures. When the reduction temperature was increased to 680°, initially a rapid rate was observed, but after a certain layer thickness had developed the rate dropped to approximately one fifth of its initial value. At 700°C, this switchover occurred after a thinner layer had formed and the rate during the second stage had a minimum value. At 720°C, the initial rate lasted for a still shorter time while the rate in the second stage similar to that observed at 700°C. When reduced at 740°C, the rapid initial rate was only just apparent and the secondary rate was now higher than that observed at 720°C. For reduction temperatures higher than 740°C, the initial rapid rate was not observed at all.

The effect of reduction pressure on the switchover point for reduction at 700°C is shown in Figure 6. Both the initial and secondary rates seemed to have a similar dependence on the hydrogen pressure.

The switchover to a slower rate was expected to be due to the formation of a protective cobalt-wüstite sub-scale, and so the microstructural development of the reduced scale was studied as a function of temperature.

2. Microstructural Observations

The structure of the reaction interface of a single crystal of cobalt ferrite partially reduced at 500°C in 30 torr hydrogen for 100s is shown in Figure 7. The micrograph clearly shows the defect free, unreacted cobalt ferrite core. The reduced metal scale is polycrystalline and porous and the pores extend right up to the reaction interface where the gas solid reaction occurs. Back from the reaction interface, the pores in the metal product layer have dynamically coarsened.

Figure 8 shows the structure of the interface of a specimen reduced at 600°C. Figure 8a shows that the nature of the porosity is different at 600°C compared with 500°C. The regular network of pores observed at 500°C is no longer in evidence, although the metal remains porous and polycrystalline. Figure 8b is a selected area diffraction pattern from a region overlapping the reaction interface. Superimposed on the matrix spinel spot pattern is a ring pattern from the polycrystalline metal scale. There was no evidence of cobalt-wüstite formation at 600°C. Figure 8c is a (111) lattice image of an interfacial region imaged at lower magnification in Figure 8a. Two interesting features are the dark regions in the lattice image, which presumably are precipitates and the apparently strained region of spinel at the interface.

The dark regions must still have a structure closely related to the spinel structure since the (111) lattice fringes are continuous across them. Presumably, these are regions where the cation content is higher than in the matrix spinel phase.

Figure 9 shows the reaction interface in a specimen reduced at 650°C. Again the porosity is coarser than that which developed at

600°C and the mechanical strains in the unreduced spinel are revealed by the nature of the bend contours. Fine precipitates ahead of the main reaction interface indicate that cation injection into the spinel has occured. However, there is no evidence of a continuous wüstite-type subscale.

The evidence for wüstite becomes more convincing when specimens are reduced at 700°C. Figure 10a shows a region in the spinel core close to the spinel-metal interface in a specimen reduced at 700°C in 30 torr of hydrogen for 60s. The small dark regions observed at 600°C have developed into recognizable coherent precipitates exhibiting coherency strain contrast. The selected area diffraction pattern associated with these regions close to the spinel core is shown in Figure 10b. The pattern has the correct spacings for a spinel structure, but the intensities of the spots alternate such that only those spots which would correspond to wüstite reflections remain bright. However, there is no splitting of the spots as would be expected if there were two clearly distinct phases present.

Figure 10c is also a diffraction pattern from a similar area in another specimen reduced at 700°C. This pattern also exhibits alternating bright and weak intensities in the spinel reflections, but, in this pattern, there are also extra reflections which, in this case, indicated a metal-oxide orientation relationship with $(100)_{\text{fcc metal}} // (311)_{CoFe_2O_4}$. These reflections would be the result of double diffraction.

During the later stages of reduction, partially reduced specimens could be examined in cross section by light microscopy. Figure 11 shows a specimen which was reduced for 240s in 100 torr of hydrogen at 700°C. After 240s, the rate of reduction had decreased. Three distinct layers can now be resolved. Adjacent to the unreduced cobalt ferrite core is a dark band, revealed by etching, which indicates a continuous wüstite subscale. To the outside of the wüstite subscale is the porous metal shell layer.

Discussion

Reaction Product Micromorphology

The kinetics of the reduction of cobalt ferrite are influenced by the microstructure of the developing reaction products and vice-versa. At low reduction temperatures, the observed effective gaseous diffusion coefficients were strongly temperature dependent. Between 400 °C and 500°C, $D_{H_2/H_2O eff}$ increased by a factor of 40, whereas a factor of about 1.3 would have been expected for molecular diffusion and even less for Knudsen diffusion, for the same scale morphology. The difference can be attributed to the coarsening of the pore network which occurs at 500°C.

The microstructure of the metal scale of the specimen partially reduced at 500°C, shown in Figure 7, exhibited a fine pore structure close to the reaction interface with a much coarser pore structure developing away from it. The very high surface area to volume ratio in the finely porous region close to the interface produced a sufficiently high driving force for coarsening that the scale rapidly transformed into the polycrystalline form with coarser intergranular pores. The pore structure close to the interface bore a strong resemblance to the structure of the magnetic scale on partially reduced hematite reported by Porter and Swann (9), indicating that such scale structures may be typical of many gas-solid reactions. The pores allowed the reducing gas to diffuse to the immediate vicinity of the chemical reaction. However, for the reaction to proceed, short-range solid state diffusion near the interface of cations to the growing metal scale and of anions to the pores is still necessary.

It is believed that below 500°C, the coarsening process takes progressively longer, forcing the reducing gases to diffuse along the very fine pores of the primary scale structure. As the reduction temperature was increased above 500°C, $D_{H_2/H_2O eff}$ decreased so that at 600°C, its value was half that observed at 500°C. This was again attributed to the increased coarsening of the scale, but this time causing some of the pores to collapse.

In the specimen reduced at 600°C, shown in Figure 8, the secondary, polycrystalline scale extended right up to the reaction interface although in Figure 9, of the specimen reduced at 650°C, there was still some evidence of the fine pores. Presumably, at these higher temperatures, significant coarsening occurs almost simultaneously with reaction. However, the specimens prepared for electron microscopy were reduced very slowly in low pressures of hydrogen. It is quite possible that specimens reduced at higher pressures of hydrogen will have an interfacial structure more closely resembling that observed at 500°C.

The lowest temperature for which there was any evidence for the presence of a wüstite-type phase was 600°C. In Figure 8c, the dark regions in the lattice image very close to the reaction interface provided evidence that the spinel structure was changing, presumably by accepting the cations rejected by the interface which did not transfer to the metal scale. However, there was no evidence of wüstite in the diffraction pattern of the interface, shown in Figure 8b.

During the early stages of reduction at 700°C, the spinel phase close to the interface was shown in Figure 10 to have changed its structure sufficiently to modify the intensities of the reflections in its diffraction pattern. In addition, clearly distinguishable coherent precipitates were imaged in Figure 10a. These precipitates are presumably the same as those observed by De Jonghe and Thomas which were shown to be precipitates of cobalt-wüstite (14).

Only during the later stages of reduction at 700°C, after reduction times sufficiently long for the reaction rate to have decreased, was a complete layer of cobalt-wüstite observed, as shown in Figure 11. There is, therefore, good evidence to correlate the reaction rate anomaly with the appearance of the continuous cobalt-wüstite layer.

The cobalt-wüstite appears to develop in the following manner at 700°C:

1) Initially, metal forms directly on the spinel surface.
2) At the same time, not all the free cations generated by the removal of oxygen from the spinel lattice transfer to the growing metal phase, some diffuse back into the spinel lattice.
3) As soon as the deviation from stoichiometry in the spinel phase is sufficiently large, discrete precipitates of cobalt-wüstite develop ahead of the advancing interface.
4) At some point, when the reaction has slowed down due to increased gas transport resistance in the scale, a continuous cobalt-wüstite layer can form, whereupon the rate will be controlled by the reduction of wüstite phase.

Effective Gaseous Diffusivity through the Metal Scale

Equation 17 could be used to analyze the kinetic data below 660°C, where the reciprocal reaction rate was found to be linearly related to the product layer thickness, ξ. Where there is both a molecular and a Knudsen component to the effective diffusion coefficient, the effective diffusion coefficient can be found from the relationship:

$$D_{H_2/H_2O\,eff}^{-1} = D_{Meff}^{-1} + D_K^{-1} \qquad 19$$

While this is a simplification for binary gaseous diffusion of different molecular weight species, it is considered to be an adequate approximation. The molecular component can also be written as

$$D_{Meff}^{-1} = \frac{P_{H_2}^{b}\,\tau}{D^{o}_{H_2/H_2O}\,\varepsilon} \qquad 20$$

Where $D^{o}_{H_2/H_2O}$ is independent of pressure. $D_{H_2/H_2O\,eff}^{-1}$ should therefore be linearly related to $P_{H_2}^{b}$, since the Knudsen diffusion coefficient, D_K, is independent of pressure. Figure 12 is a plot of $D_{H_2/H_2O\,eff}^{-1}$ versus $P_{H_2}^{b}$ at 600°C. It is clear that both Knudsen and molecular transport contribute to the observed effective gaseous diffusion coefficient and their relative contributions can be deduced from Figure 12. The binary diffusion coefficient, D_{H_2/H_2O}, can be readily established from gas diffusion theory and values for different temperatures have been calculated in Appendix 3. From Figure 12 and equations 19 and 20, taking the porosity, ε, as 0.35, assuming zero shrinkage, a value of 23 for the tortuosity, τ, is obtained. Due to increasing coarsening with increased temperature, changes in τ are to be expected that are related to the pore morphology. However, Rey and De Jonghe showed that significant morphology changes were not correlated with the reaction rate anomoly (2).

The Interface Reaction

It is clear from the values of the reaction rate constant, k_r, listed in Table 2, that k_r is a function of pressure. Figure 13 is a plot of k_r^{-1} against pressure, which shows that, when analyzed in terms of equation 18, k_r followed Langmuir-Hinshelwood kinetics. In this section, an interface process is considered which leads to such kinetics. The interface reaction considered is shown in Figure 14. The gaseous hydrogen molecules combine with the surface oxygen to form water, producing an excess of cations in the surface. The excess metal cations will have to diffuse to the metal phase sink. At the same time, in order for the reaction interface to advance, oxygen ions must be removed from the metal/metal oxide interface while the cations produced there are deposited on the metal phase. The oxygen ions have to diffuse to the pore surface and combine with hydrogen. The interface reaction process is clearly a very complex one, even if all surface reactions including adsorption, desorption, and electronic processes are in equilibrium. We assume that the entire solid-state diffusion process is dominated by the excess cations, (M), generated at the pore, which give rise to the oxygen ion and metal ion fluxes. This total flux is thus taken to be simply proportional to the excess cation concentration [(M)]. One can then describe the process as depicted in Figure 14 by the following reaction:

$$H_2(g) \quad + \quad (OM) \underset{k_{-1}}{\overset{k_1}{\rightleftharpoons}} H_2O(g) + (M) \qquad 21$$

If [(OM)] is the fraction of active surface sites presenting oxygen to the gas phase and [(M)] is the fraction of excess cations, we can write:

$$[(OM)] \quad + \quad [(M)] \quad = \quad 1 \qquad 22$$

Assuming, as was done for equation 17, that the reverse reaction is negligible, we can write:

$$J(0) = \frac{k_1 \, p^b_{H_2} \, [(OM)]}{RT} \qquad 23$$

and $$J(0) = k_3 \, [(M)] = B^* \frac{D_{ss}}{\lambda} \, [(M)] \qquad 24$$

Where B^* is a proportionality constant, D_{ss} is a solid-state diffusion coefficient and λ is the average source to sink distance. Equation 24 implies that solid-state diffusion occurs in a constant geometry throughout the reaction process and is a statement of Fick's law.

From equation 22-24, it follows that:

$$J(0) = \frac{k_3 RT}{\frac{k_3 RT}{k_1} + p^b_{H_2}} \; \frac{p^b_{H_2}}{RT} \qquad 25$$

Using the notation of equation 18, this becomes:

$$J(0) = \frac{k'}{k'' + p^b_{H_2}} \; \frac{p^b_{H_2}}{RT} \qquad 26$$

This expression does indeed describe Langmuir-Hinshelwood kinetics and the chemical rate constant, k_r, is:

$$k_r = \frac{k_3 RT}{\frac{k_3 RT}{k_1} + p^b_{H_2}} \qquad 27$$

The chemical rate constant might also be written in Arrhenius form

if $p^b_{H_2} << \frac{k_3}{k_1} RT$. i.e.,

$$k_r = k_o \exp\left(\frac{-Q}{RT}\right) \qquad 28$$

While this condition is not fully satisfied at 100 torr, one can still obtain a reasonably linear relationship between $\ln k_r$ and T^{-1}, as shown in Figure 15. A value of 18 k cal mole^{-1} is obtained below 660°C, where equation 17 is valid. This value should be close to the activation energy of the chemical reaction rate parameter, k_1. The actual value of k_1 as a function of temperature can in principle be obtained from the values of k_r extrapolated to $p^b_{H_2} = 0$ but these experiments have not been carried out for the full range of temperatures. The pressure dependence of k_r at 600°C is shown in Figure 13 from which the Langmuir-Hinshelwood parameters k' and k'' can be established. At 600°C, it was found that $k' = 1337$ cm torr sec^{-1} and $k'' = 115$ torr. It is clear, however, from the previous discussion and equation 27 that a simple, fundamental meaning cannot readily be assigned to k' and k''.

The parameter $k_3 = B^* D_{ss}\, \lambda^{-1}$ plays an important part in the degree to which the interface reaction appears non-linear in its pressure dependance in the pressure range studied. From equation 25 it follows that if $D_{ss} << p^b_{H_2} \frac{\lambda k_1}{B^* RT}$, k_r should appear independent of pressure. One might thus predict that the Langmuir-Hinshelwood kinetics may be apparent in quite different pressure regimes depending on the solid-state diffusion rates. If, for example, alloying elements are present which depress the diffusion rate of the relevant ions, then the interface reaction rate constant, k_r, will be less pressure dependent.

It is interesting to note that if the interface reaction rate had been pressure independent and the mass transfer resistance significant, Langmuir-Hinshelwood kinetics would again have been observed. In such a situation, k_1 in Equation 23 would have to be replaced by $(k_1^{-1} + k_m^{-1})^{-1}$. Since k_m is inversely proportional to pressure, an expression for J(0) of the same form as equation 26 would result. However, the very low mass transfer resistance that was calculated precludes this possibility.

The Reaction Rate Anomaly and the Incubation Time

The reaction rate anomaly observed between 600°C and 800°C cannot be correlated with the temperature at which the cobalt-wüstite phase first becomes stable. This lack of correspondence cannot be attributed to a large nucleation barrier since De Jonghe and Thomas (14) observed that cobalt-wüstite nucleated readily during the reduction of cobalt ferrite, even at temperatures as low as 500°C. The data presented here showed that the reaction rate anomaly is indeed caused by the formation of a continuous cobalt-wüstite subscale which may be absent in the early part of the reduction in the reaction rate anomaly temperature range. It is argued that this apparent "incubation period," in which a continuous wüstite layer was found to be absent in the transmission electron microscope, as well as the temperature at which the reaction rate anomaly occurs is of a kinetic origin. The rate of growth, v_{sw}, of a small cobalt-wüstite precipitate at the metal/spinel interface, shown schematically in Figure 16, is compared with the rate of advance of that interface, $\dot{\xi}$. If the particle is consumed by the advancing interface more rapidly than it can grow, then a continuous wüstite layer cannot form. It is considered that while the cobalt-wüstite precipitates may be nucleated ahead of the advancing spinel/metal interface, their growth would only be rapid when in contact with it.

Thus, the rate of growth should depend on the chemical potential difference, $\Delta\mu$, between the metal/wüstite interface and the spinel/metal interface. The velocity of the spinel/wüstite interface, v_{sw}, is therefore expected to be of the form:

$$v_{sw} = A^{*} \exp\,(-\,Q_w/RT)\,.\,\Delta\mu. \qquad 29$$

For simplicity, the particle size dependence of v_{sw} has been neglected. This is probably not too drastic a simplification when the particle size is small and interface reaction rates rather than diffusional rates determine v_{sw}. v_{sw} is then compared with $\dot{\xi}$ in equation 17. If $v_{sw} < \dot{\xi}$ a continuous subscale cannot form. The critical layer thickness ξ_c at which $v_{sw} = \dot{\xi}$ is then

$$\xi_c = \frac{D_{H_2/H_2O\,eff}\; p^{b}_{H_2}}{RT} \left[\left(c_0\, A^{*}\, \Delta\mu \exp\left(\frac{-Q_w}{RT}\right)\right)^{-1} - \frac{RT}{k_r p^{b}_{H_2}} \right] \qquad 30$$

near 800°C, where the reduction rate data indicate that $\xi_c = 0$, the solid state diffusion rates near the spinel/metal interface are expected to dominate the interface reaction so that equation 27 simplifies to:

$$k_r = \frac{k_3 RT}{p^{b}_{H_2}} \qquad 31$$

Thus, $\xi_c = 0$, corresponding approximately to the minimum in the reaction rate for short reaction times, will occur at the pressure independent temperature:

$$T_o = -\,\frac{Q_w}{R\,\ln(k_3/c_0 \Delta\mu\, A^{*})} \qquad 32$$

At a fixed temperature somewhat below T_o, according to equation 30, ξ_c will increase with increasing $p^b_{H_2}$. Since all the kinetic parameters are not known, only the qualitative behavior of ξ_c has been sketched in Figure 17. As is apparent from this figure, the reduction rate will be characteristic of the direct spinel/metal reaction until $\xi = \xi_c$. At that point, the reaction rate should become characteristic of the spinel/wüstite metal reaction. For a fixed $p^b_{H_2}$, the maximum rates for complete reduction will occur when the specimen sizes are less than twice the critical layer thickness. For example, from Figure 6 it is clear that at 200 torr, a maximum particle size for optimum complete reduction rates will be approximately 0.2mm.

It is worthwhile to emphasize the role of the solid state rate processes characterized by the rate parameter k_3 and A^*. If the solid state transport rates in the spinel-to-wüstite transformation is depressed by alloying additions to the spinel, then $\overset{*}{A}$ may decrease more rapidly than k_3, thereby shifting T_o to a higher temperature. This follows from equation 30. This was indeed observed by Rey and De Jonghe (2) for Al^{3+} containing cobalt ferrites.

The Overall Reaction

The experiments have demonstrated that in the temperature regime for which the interfacial reaction mechanism does not change significantly, equation 17 holds and can be used to establish the kinetic parameters k_r and D_{H_2/H_2Oeff} for those conditions. It is then possible to use these kinetic constants to calculate reaction rates for different, more complicated, specimen geometries and reactor conditions. For example, the general model developed by Szekeley, Evans, and Sohn can be used to predict the experimental results for reduction using the kinetic constants obtained by using equation 17. This has been done for reduction in 100 torr of hydrogen at 600°C in Appendix 4. Equation 17 only breaks down when the spinel-metal interface slows down sufficiently such that a dense wüstite layer can develop. However, the experiments still allow a prediction to be made concerning the optimum particle size for maximum reduction rates for the temperature regime in which wüstite can develop.

Summary

1) Below 660°C, the reduction of cobalt ferrite by hydrogen at reduced pressures was shown to be under the mixed control of the chemical reaction at the scale/cobalt ferrite interface and of gaseous diffusion through the scale.

2) The effective gaseous diffusion coefficient for diffusion through the scale was shown to have both Knudsen and molecular components and it was shown to have a maximum value at 500°C. The changes in the diffusion coefficient as a function of the reducing conditions were attributed to changes in the scale micromorphology.

3) The interface reaction rate constant was shown to follow Langmuir-Hinshelwood kinetics. A model incorporating a solid-state diffusion step was derived to explain such a pressure dependance of the rate constant. The activation energy for the chemical reaction was shown to be 18 kcal/mole.

4) The reaction rate minimum as a function of temperature, which was observed at 700°C, was caused by the development of a continuous sub-scale of cobalt-wüstite. The incubation period for the development of the subscale was explained in terms of the different velocities of the spinel-metal interface and the spinel-wüstite interface. A critical layer thickness was defined as the thickness of the metal scale at the moment when the subscale became continuous. The temperature and pressure dependence of the critical layer thickness was discussed.

ACKNOWLEDGMENT

This work was supported by the Division of Materials Sciences, Office of Basic Energy Sciences, U. S. Department of Energy, under contract No. W-7405-Eng-48.

References

1. R. H. Spitzer, F. S. Manning, and W. O. Philbrook; Trans. TMS-AIME, 1966, Vol. 236, pp. 726-742.
2. M. C. Rey and L. C. De Jonghe; Submitted to Met. Trans. B.
3. E. T. Turkdogan and J. V. Vinters; Met. Trans. B, 1971, Vol. 2, pp. 3175-3188.
4. J. M. Quets, M. E. Wadsworth and J. R. Lewis; Trans. TMS-AIME, 1961, Vol. 221, pp. 1186-1193.
5. K. R. Lilius; Acta Polytech. Scand., 1974, ch. 118, pp. 6-18.
6. J. Szekely, J. W. Evans and H. Y. Sohn, Gas-Solid Reactions, Academic Press, 1976.
7. W. M. McKewen, Trans. TMS-AIME, 1962, Vol. 224, pp. 387-393.
8. P. R. Swann and N. J. Tighe; Met. Trans. B, 1977, Vol. 8B, pp. 479-487.
9. J. R. Porter and P. R. Swann, Ironmaking and Steelmaking, 1977, Vol. 4, pp. 300-307.
10. R. G. Olsson and W. M. McKewan, Trans. TMS-AIME, 1966, Vol. 236, pp. 1518-1522.
11. R. G. Olsson and W. M. McKewan, Met. Trans., 1970, Vol. 1, pp. 1507-1512.
12. J. K. Galt, B. T. Matthias, and J. P. Remeika; Phys. Rev., 1950, Vol. 79, pp. 391-396.
13. R. B. Bird, W. E. Stewart, and E. N. Lightfoot; Transport Phenomena, Wiley, 1960.
14. L. C. De Jonghe and G. Thomas; Mater. Sci. Eng., 1971, Vol. 8, pp. 259-274.

Appendix 1

Relationship Between Measured Weight Loss And Calculated Shell Layer Thickness

This relationship assumes that the reduction is topochemical and that there is no overall volume change on reduction.

Let volume of slab, $V\ (o) = a_1\ a_2\ a_3$ 33

where a_1 a_2 and a_3 are the side lengths of the slab 34

Then, the volume of the core, $V(\text{core}) = (a_1 - 2\xi)\ \ (a_2 - 2\xi)\ \ (a_3 - 2\xi)$

where ξ is the shell layer thickness.

By subtraction, the volume of the metal shell, $V(\text{shell}) = V(o) - V(\text{core})$

$$= 2\xi(a_2a_3 + a_1a_3 + a_1a_2) - 4\xi^2\ (a_1+a_2 + a_3) + 8\xi^3$$

Since ξ is small, $8\xi^3$ can be neglected. 35

Now
$$\frac{WL}{WL_{max}} = \frac{V(\text{Shell})}{V(o)} \qquad 36$$

$$WL = \frac{WLmax}{abc}\ 2\xi\ (a_2a_3 + a_1a_3 + a_1a_2) - 4\xi^2(a_1 + a_2 + a_3))$$

This quadratic equation can be solved for the positive value of ξ. 37

Appendix 2

Calculation of the Exhaust p_{H_2}/p_{H_2O} Ratio for Maximum Observed Reaction Rate

Bulk gas flow rate, measured at 760 torr and 20°C $= 25 \text{ ml s}^{-1}$

$$= \frac{25}{22400} \text{ moles s}^{-1}$$

$$= 1.116 \times 10^{-3} \text{ moles s}^{-1}$$

The molar flow rate is independent of temperature and pressure.

The maximum observed shell layer growth rate, $\dot{\xi}_{max}$, was 0.0002 cm s^{-1}

The surface area of a typical specimen 2 cm^2

Now, molar density of $CoFe_2O_4$ $\rho_s = \frac{5.3}{234.63}$ moles cm^{-3}

$$= 2.26 \times 10^{-2} \text{ moles cm}^{-3}$$

$\therefore$ atomic concentration of oxygen in $CoFe_2O_4$, $c_O = 4 \times 2.26 \times 10^{-2}$ g atom O_2 cm^{-3}

$$= 0.09 \text{ g atom } O_2 \text{ cm}^{-3}$$

$\therefore$ Max rate of consumption of oxygen by reaction $= 0.09 \times 0.0002 \times 2$ g atom O_2 cm^{-3}

$$= 3.6 \times 10^{-5} \text{ g atom } O_2 \text{ cm}^{-3}$$

Since one mole hydrogen reacts with one gram atom oxygen:

Molar rate of reaction $= 3.6 \times 10^{-5} \text{ moles s}^{-1}$

$$\therefore \text{ the exhaust } \frac{p_{H_2}}{p_{H_2O}} \text{ ratio} = \frac{1.116 \times 10^{-3} - 3.6 \times 10^{-5}}{3.6 \times 10^{-5}}$$

$$= 31/1$$

Appendix 3

Calculation of the External Mass Transfer Coefficient, k_m, for reduction in torr hydrogen at 500°C, 600°C, 700°C, and 800°C.

The mass transfer coefficient is calculated from a knowledge of the Sherwood number, which, in turn, is a function of the Reynolds number and the Schmidt number.

The Schmidt number, $N_{SC} = \frac{\mu}{\rho D}$

An estimate of D_{H_2/H_2O} can be made using the Chapman-Enskog equation:

$$D_{H_2/H_2O} = \frac{1.8583 \times 10^{-3} \sqrt{T^3\left(\frac{1}{M_{H_2}} \quad \frac{1}{M_{H_2O}}\right)}}{p\sigma^2_{H_2/H_2O}\Omega_{H_2/H_2O}} \qquad 38$$

Now $\sigma_{H_2/H_2O} = 1/2\ (\sigma_{H_2} + \sigma_{H_2O})$

and $\Omega_{H_2/H_2O} = f\ \frac{T}{(\Sigma_{H_2/H_2O}/K)}$ for which values are tabulated (13)

$$\frac{\Sigma_{H_2/H_2O}}{K} = \sqrt{\left(\frac{\Sigma_{H_2}}{K}\right)\left(\frac{\Sigma_{H_2O}}{K}\right)}$$

Density of the reducing gas, $\rho = \frac{pM}{RT}$ and values for the viscosity, μ are tabulated. Values for viscosity are considered to be independent of gas pressure. The Reynolds number, $N_{Re} = \frac{LV\rho}{\mu}$.

The specimen dimension L, was taken as 0.5 cm and the gas velocity in the tube was calculated from a knowledge of the measured flow rate of the gas at ambient temperature and pressure, the cross sectional area of the furnace work tube and the ideal gas law. The measured gas flow rate was 24 ml s^{-1} and the work tube cross sectional area was 5 cm^2. The Sherwood number,

$$N_{Sh} = 2 + 0.6\ N_{Re}^{1/2}\ N_{Sc}^{1/3}$$

Also, by definition, $N_{Sh} = \frac{k_m L}{D}$, from which values for the external mass transfer coefficient can be calculated. The calculations are set out in Table 3.

Appendix 4

The reaction constant obtained from the analysis can be used to predict rates for other particle geometries using the general rate expression developed by Szekeley, Evans, and Sohn (6). The general expression relating conversion and time in a dimensionless form, for the reaction

$$A + bB = C + dD \tag{39}$$

is: $$t^{*} = g_{F_p}(X) + \sigma_s^2 \left[P_{F_p}(X) + 2\,X/N_{Sh}^{*}\right] \tag{40}$$

Where $$t^{*} = \frac{b\,k_r (c_{A_o}^{b} - \frac{c_{C_o}^{b}}{K_e}}{R_o\,\rho_s}\,t \tag{41}$$

$$g_{F_p}(X) = 1 - (1-X)^{1/F_p} \tag{42}$$

$$P_{F_p}(X) = 3 - 3\,(1-X)^{2/3} - 2X \qquad \text{for } F_p = 3 \tag{43}$$

$$= X + (1-X)\ln(1-X \qquad \text{for } F_p = 2 \tag{44}$$

$$= X^2 \qquad \text{for } F_p = 1 \tag{45}$$

F_p is a shape factor and has a value of 3 for spheres, 2 for long cylinders and 1 for slabs.

$$\sigma_s^2 = \frac{k_r\,R_o}{2F_p D_{Aeff}} \left(1 + \frac{1}{K_e}\right) \tag{46}$$

$$N_{Sh}^{*} = \frac{k_m\,R_o}{2D_{Aeff}} \tag{47}$$

The equation for the reduction of cobalt ferrite by hydrogen is:

$$H_2 + \frac{1}{4}\,CoFe_2O_4 = H_2O + \frac{1}{4}\,CoFe_2$$

For the slab geometry used in the present experiments, $F_p = 1$ and R_o is taken as the half thickness of the slab.

This model can be used to predict the extent of reaction with time, and for the reduction of cobalt ferrite in hydrogen at 600°C at 100 torr, the values of the dimensionless parameters are as follows:

Calculation of N_{Sh}^{*}:

R_o = 0.032 cm

k_m = 215 cm s^{-1}

D_{Aeff} = 0.2 cm^2 s^{-1}

N_{Sh}^{*} = 17.2

Calculation of σ_s^2:

k_r = 6.21 cm s^{-1}

K_e >> 1

σ_s^2 = 0.496

Calculation of t^*:

b = 0.25

c_A^b = 1.84×10^{-6} mole cm^{-3}

c_C^b ≃ 0

ρ_s = 2.26×10^{-2} mole cm^{-3}

t^* = 3.95×10^{-3} t

Therefore, the general expression simplifies to:

$$t = 239X + 126X^2 \text{ s} \qquad (48)$$

This equation relating time to the extent of reaction has been compared with the observed rate of reaction in Figure 18. The data are given in table 4.

Table 1

REDUCTION PARAMETERS FOR REDUCTION AT 100 TORR

Temperature (^oC)	$\frac{1}{T}$ (K^{-1})	$\dot{\xi}_o^{-1}$ ($cm\ s^{-1})^{-1}$	k_r ($cm\ s^{-1}$)	$\ln k_r$ ($\ln(cm\ s^{-1})$)	$\frac{\dot{\xi}^{-1}}{\xi}$ ($cm^2 s^{-1})^{-1}$	$D_{H_2/H_2O eff}$ ($cm^2 s^{-1}$)
400	.00149	188132	0.201	-1.604	3308439	0.0114
460	.00136	57690	0.713	-0.338	606543	0.0678
480	.00133	28601	1.48	0.392	134171	0.314
500	.00129	20709	2.10	0.742	98256	0.440
540	.00123	11456	3.99	1.384	223034	0.204
600	.00115	7895	6.21	1.826	245087	0.199
620	.00112	5829	8.61	2.153	419212	0.119
640	.00109	6823	7.52	2.017	401862	0.127
650	.00108	5827	8.9	2.186	393984	0.131
660	.00107	4605	11.38	2.432	333288	0.156

Table 2

REDUCTION PARAMETERS FOR REDUCTION AT 600°C

Pressure (torr)	ξ_0^{-1} $(\mathrm{cm\ s^{-1}})^{-1}$	k_r $(\mathrm{cm\ s^{-1}})$	k_r^{-1} $((\mathrm{cm\ s^{-1}})^{-1})$	$\frac{\dot{\xi}^{-1}}{\xi}$ $((\mathrm{cm^2 s^{-1}})^{-1})$	$D_{H_2/H_2O\mathrm{eff}}$ $(\mathrm{cm^2 s^{-1}})$	$D_{H_2/H_2O\mathrm{eff}}^{-1}$
50	12695	7.72	0.129	409309	0.239	4.18
100	7895	6.21	0.161	245087	0.199	5
125	6594	5.94	0.168	249937	0.157	6.38
200	5999	4.08	0.245	179283	0.137	7.32
250	5313	3.69	0.271	142257	0.138	7.26

Table 3

DATA USED IN THE CALCULATION OF THE MASS TRANSFER COEFFICIENT

Parameter	Value			
Temperature (°C)	500	600	700	800
Temperature, T (K)	773	873	973	1073
$\frac{TK}{\Sigma_{H_2/H_2O}}$	3.51	3.97	4.42	4.88
Ω_{H_2/H_2O}	0.912	0.884	0.865	0.846
Pressure, p (atmos)	0.132	0.132	0.132	0.132
Diffusivity, D_{H_2/H_2O} (cm^2 S^{-1})	33.1	40.1	49.3	58.3
Viscosity, μ(g cm^{-1} s^{-1}) (from tables)	1.68×10^{-4}	1.82×10^{-4}	1.96×10^{-4}	2.1×10^{-4}
Density, ρ (g cm^{-3}) (for hydrogen)	4.16×10^{-6}	3.68×10^{-6}	3.31×10^{-6}	3×10^{-6}
Schmidt Number, N_{Sc}	1.22	1.23	1.2	1.2
Gas Velocity, V (cm s^{-1})	97.9	110.6	123.2	135.9
Specimen Dimension, L (cm)	0.5	0.5	0.5	0.5
Reynolds Number, N_{Re}	1.21	1.12	1.04	0.97
Sherwood Number, N_{Sh}	2.7	2.68	2.65	2.63
Mass transfer coefficient, km (cm s^{-1})	179	215	261	307

Table 4

Comparison of dimensionless parameter model with experimental data for reduction at 600°C in 100 torr hydrogen.

Model		Experiment		
X	t (s)	t (s)	ξ (cm)	X
0	0	60	0.00504	0.16
0.1	25	84	0.00756	0.24
0.2	53	120	0.01104	0.35
0.3	83	180	0.01623	0.51
0.4	116	240	0.02093	0.65
0.5	151	300	0.02528	0.79
0.6	189	360	0.02897	0.91
0.7	229	420	0.03200	1.00
0.8	272			
0.9	317			
1.0	365			

LIST OF SYMBOLS

Symbol		Units
a_1, a_2, a_3	Side lengths of specimen	cm
a^*	Constant in Langmuir-Hinshelwood rate equation	cm s^{-1}
A	Component of a general chemical reaction	
A^*	Constant as defined by equation 29	cm mole $kcal^{-1}$ s^{-1}
b	Constant in general chemical reaction equation	
b^*	Constant in Langmuir-Hinshelwood rate equation	cm^3 g $mole^{-1}$
B	Component in a general chemical reaction	
B^*	Proportionality constant in equation 24	g atom O_2 cm^{-3}
c_i	Concentration of component i	g mole cm^{-3}
c_i^b	Concentration of component i in bulk gas stream	g mole cm^{-3}
c_i^i	Concentration of component i at reaction interface	g mole cm^{-3}
c_i^o	Concentration of component i at specimen surface	g mole cm^{-3}
c_0	Concentration of oxygen in oxide	g atom O_2 cm^{-3}
C	Component in a general chemical reaction	
d	Constant in general chemical reaction equation	
D	Component in a general chemical reaction	
D_{ij}	Binary diffusion coefficient	cm^2 s^{-1}
D_{ij}^o	Pressure independent diffusion coefficient defined by equation 20	cm^2 torr s^{-1}
D_{ijeff}	Effective binary diffusion coefficient	cm^2 s^{-1}
D_{k-}	Knudsen diffusion coefficient	cm^2 s^{-1}
D_{Meff}	Effective molecular diffusion coefficient	cm^2 s^{-1}

Symbol		Units
D_{ss}	Solid-state diffusion coefficient	$cm^2\ s^{-1}$
F_p	Shape factor	
g_{F_p}	Conversion function	
$J(H_2)$	Flux of hydrogen	g mole $cm^{-2}\ s^{-1}$
$J(H_2O)$	Flux of water vapor	g mole $cm^{-2}\ s^{-1}$
$J(O)$	Flux of oxygen	g atom $O_2\ cm^{-2}\ s^{-1}$
k_1	Forward chemical reaction rate constant	$cm\ s^{-1}$
k_{-1}	Reverse chemical reaction rate constant	$cm\ s^{-1}$
k_3	Rate constant for solid-state diffusion as defined in equation 24.	g atom $O_2 cm^{-2}\ s^{-1}$
k'	Langmuir Hinshelwood rate constant	cm torr s^{-1}
k''	Langmuir Hinshelwood rate constant	torr
k_m	External mass transfer coefficient	$cm\ s^{-1}$
k_o	Pre exponent as defined by equation 28	$cm\ s^{-1}$
k_r	Chemical rate constant for overall chemical reaction	$cm\ s^{-1}$
K_e	Equilibrium constant	
L	Specimen dimension	cm
M_i	Molecular weight of species i	
N_{Re}	Reynolds number	
N_{Sc}	Schmidt number	
N_{Sh}	Sherwood number	
N_{Sh}^*	Modified Sherwood number	

p_i^b	Pressure of component i in bulk gas stream	atmos. or torr
p_i	Pressure of component i	torr
p_{F_p}	Conversion function	
Q	Activation energy for the chemical rate constant	k cal mole^{-1}
Q_w	Activation energy for spinel-wüstite interface advance	k cal mole^{-1}
R	Gas constant	
R_o	Half thickness of slab	cm
t	Time	s
t^*	Dimensionless time	
T	Temperature	K
T_o	Pressure independent temperature defined by equation 32	K
v_{sw}	Rate of spinel-wüstite interface growth	cm s^{-1}
V	Bulk gas velocity	
V (core)	Volume of unreduced ferrite core	cm^3
V (o)	Initial volume of specimen	cm^3
V (shell)	Volume of metal shell layer	cm^3
WL	Instantaneous weight loss	mg
WL_{max}	Weight loss after total reduction	mg
X	Fractional extent of reaction	
ε	Porosity	
$\varepsilon_{i/k}$	Lennard-Jones parameter for component i	K
ξ	Metal scale thickness	cm (or mm)
ξ_c	Critical layer thickness	cm
$\dot{\xi}$	Metal scale growth rate	cm s^{-1} (or mm s^{-1})
$\dot{\xi}_o$	Initial rate of scale growth	cm s^{-1}

λ	Source to sink distance for solid state diffusion	cm
μ	Viscosity	g cm^{-1} s^{-1}
$\Delta\mu$	Chemical potential difference	k cal $mole^{-1}$
ρ	Density	g cm^{-3}
ρ_s	Molar density of solid	moles cm^{-3}
σ_i	Lennard-Jones parameter for component i	Å
σ_s	Reaction modulus	
τ	Tortuosity	
Ω_{ij}	Lennard-Jones collision integral	

Figure Captions

Figure 1	Schematic diagram of the thermogravimetric analysis apparatus. XBL 794-9305
Figure 2	Reduction kinetics of cobalt ferrite slabs in 100 torr hydrogen showing the anomolous reaction rate minimum. XBL 791 7743.
Figure 3	Reduction kinetics at 100 torr for specimens reduced between 500°C and 680°C. Plotted as the reciprocal interface advance rate against the extent of reaction. XBL 792 8370
Figure 4	Reduction kinetics at 600°C for specimens reduced at different pressures between 50 torr and 250 torr. a) Plotted as the extent of reaction against time. b) plotted as the reciprocal rate of reaction against the extent of reaction. a) XBL 794-9427 b) XBL 794-9428
Figure 5	Reduction kinetics at 100 torr for specimens reduced between 660°C and 740°C. XBL 794-9429
Figure 6	Reduction kinetics at 700°C for specimens reduced between 50 torr and 200 torr. XBL 794-9426
Figure 7	TEM image of the reaction interface region a partially reduced single crystal of cobalt ferrite reduced at 500°C in 30 torr hydrogen for 100s. XBB 794-5196
Figure 8	The interfacial region of a specimen reduced at 600°C in 30 torr hydrogen for 100s. a) Bright field image of interface. b) Selected area diffraction pattern of a region including the interface. c) lattice image of the cobalt ferrite adjacent to the interface, XBB 796-7766
Figure 9	Reaction interface of a specimen reduced at 650°C in 30 torr hydrogen for 60s. XBB 794-5195

Figure 10	a) Coherent precipitates in spinel region close to the interface after reduction at 700°C in 30 torr hydrogen for 60s. b) Selected area diffraction pattern showing alternating intensities. c) Selected area diffraction pattern showing the appearance of new reflections. XBB 796-7768
Figure 11	Light micrograph of a partially reduced polycrystalline slab after etching to reveal a dark band of wüstite at the reaction interface. The specimen was reduced at 700°C in 100 torr hydorgen for 240s. XBB 796-7767
Figure 12	The effective H_2/H_2O diffusion coefficient as a function of bulk hydrogen pressure. XBL 796-10121
Figure 13	The reciprocal reaction rate constant as a function of pressure showing that the rate follows Langmuir-Hinshelwood kinetics. XBL 796-10122
Figure 14	Schematic diagram of the interface reaction. XBL 796-10416
Figure 15	Arrhenius plot for the chemical reaction rate constant. The activation energy was 18.1 kcal mole^{-1}. XBL 796-10123
Figure 16	Schematic diagram of the development of a cobalt-wüstite precipitate. XBL 797-10735
Figure 17	Qualitative behavior of ξ_c as a function of temperature. XBL 798-11035
Figure 18	A comparison of the dimensionless parameter rate equation with the experimental data for reduction at 600°C in 100 torr hydrogen. XBL 796-10124

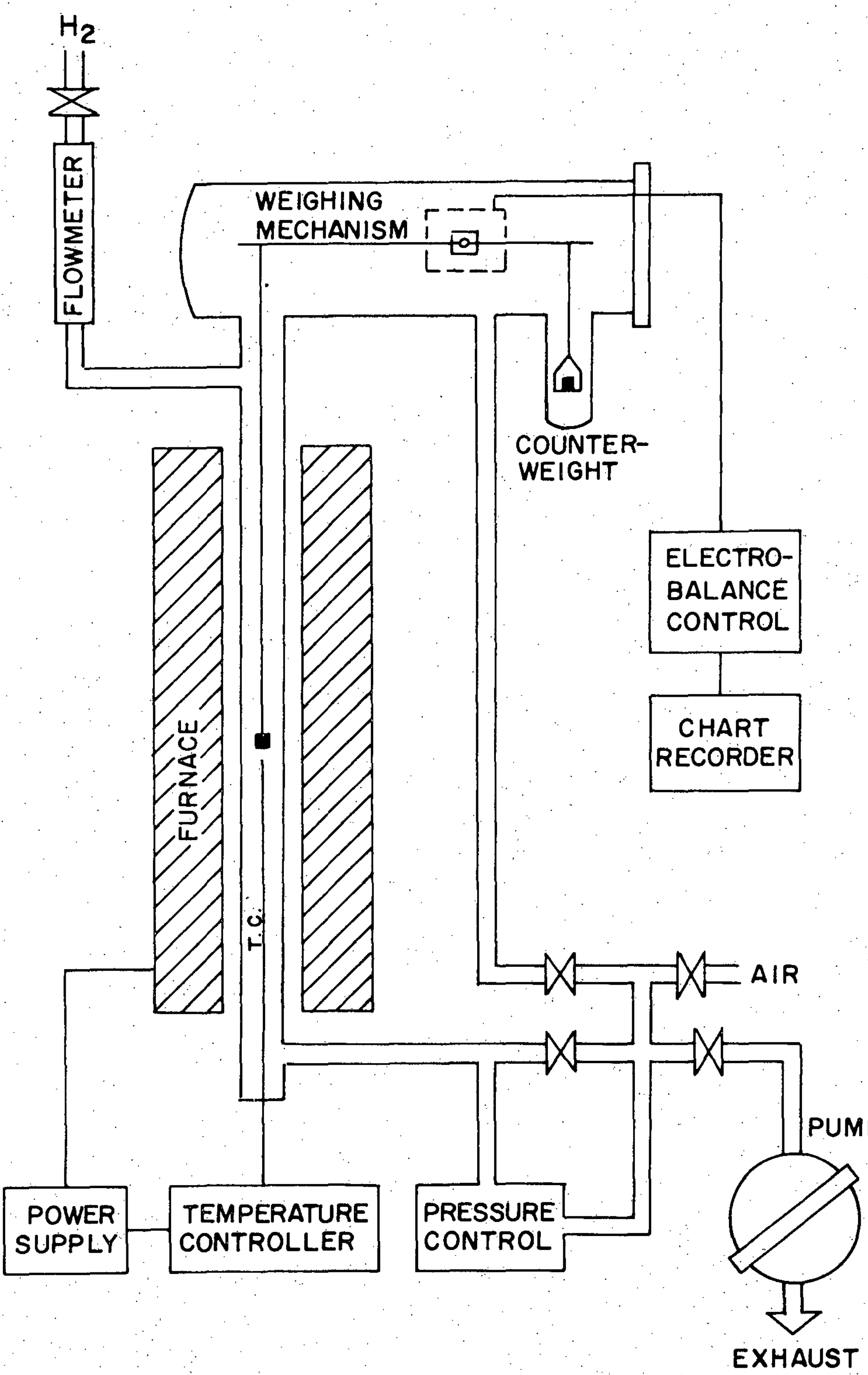

XBL 794-9305

Figure 1

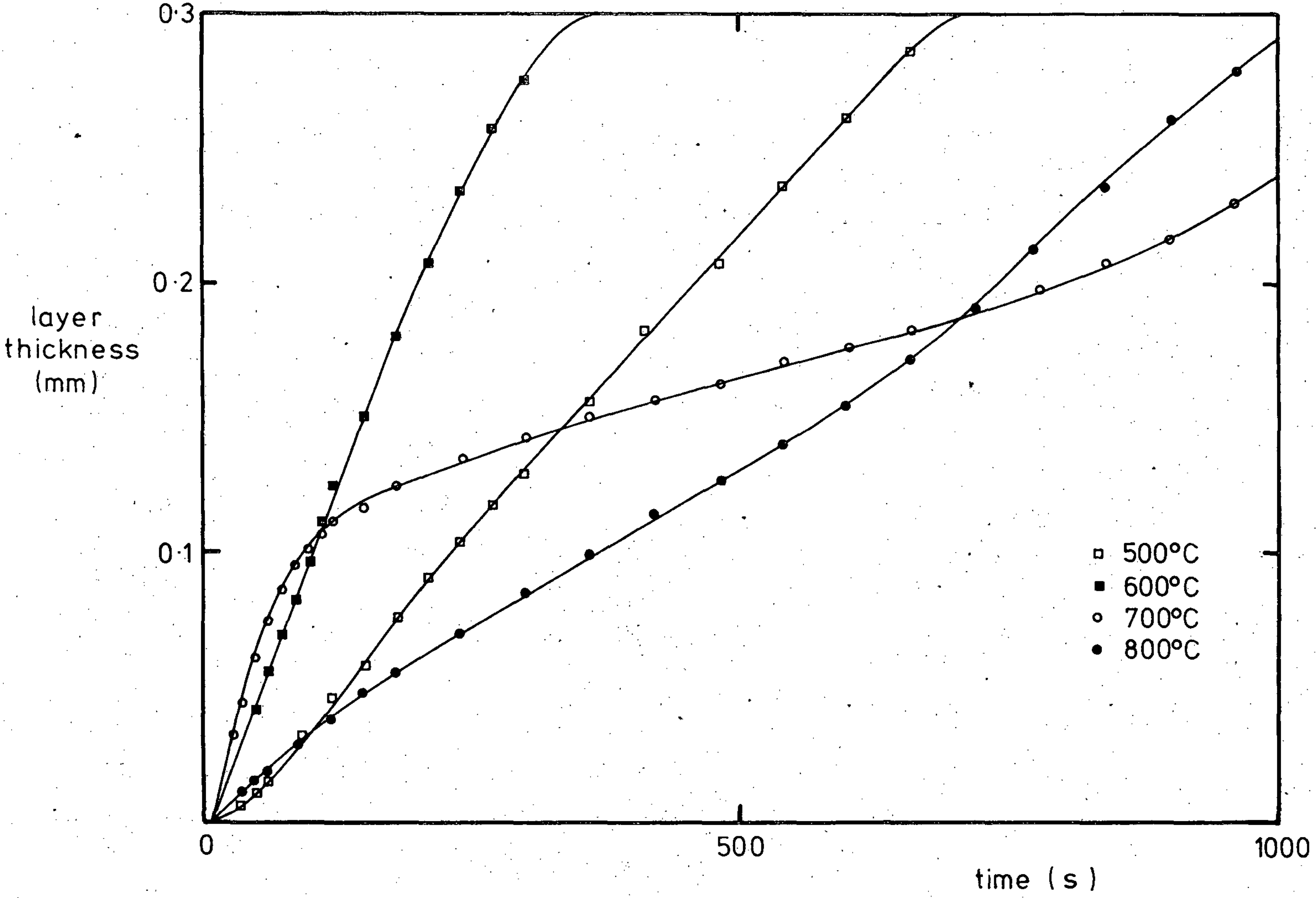

XBL 791-7743

Figure 2

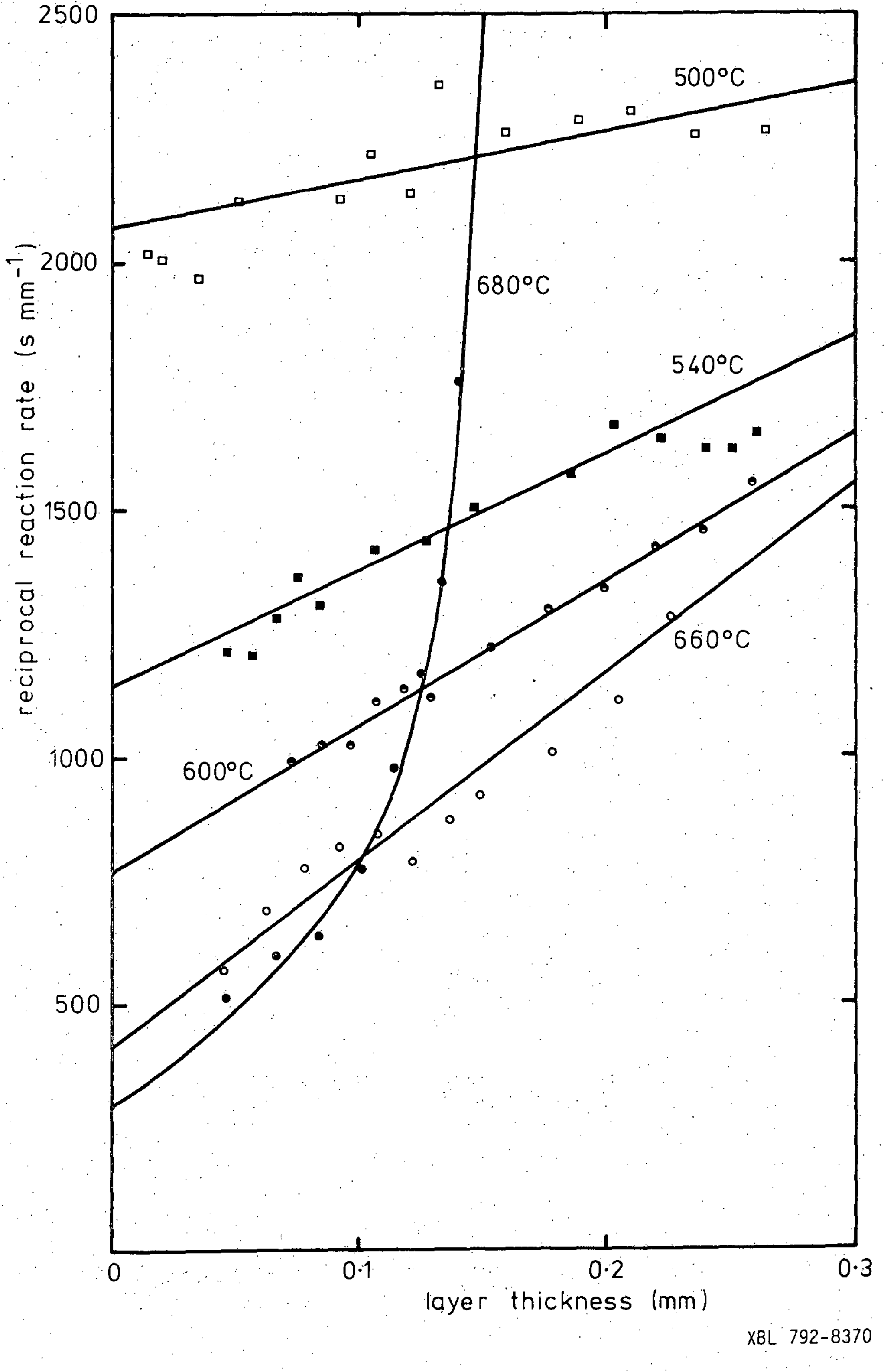
2500
2000
1500
1000
500
0
0·1
0·2
0·3
reciprocal reaction rate (s mm^{-1})
layer thickness (mm)
500°C
680°C
540°C
600°C
660°C
XBL 792-8370

Figure 3

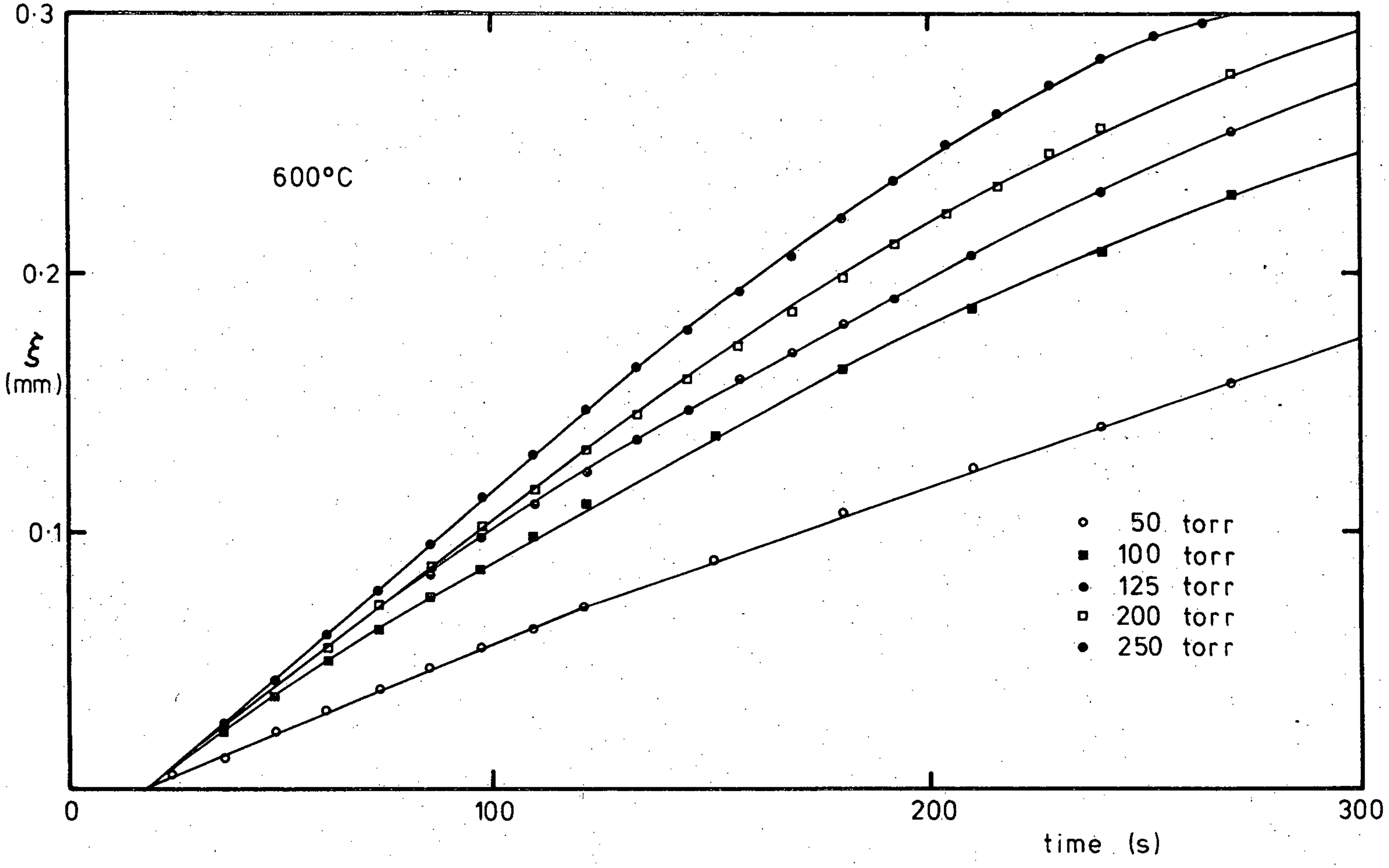

XBL 794-9427

Figure 4 (a)

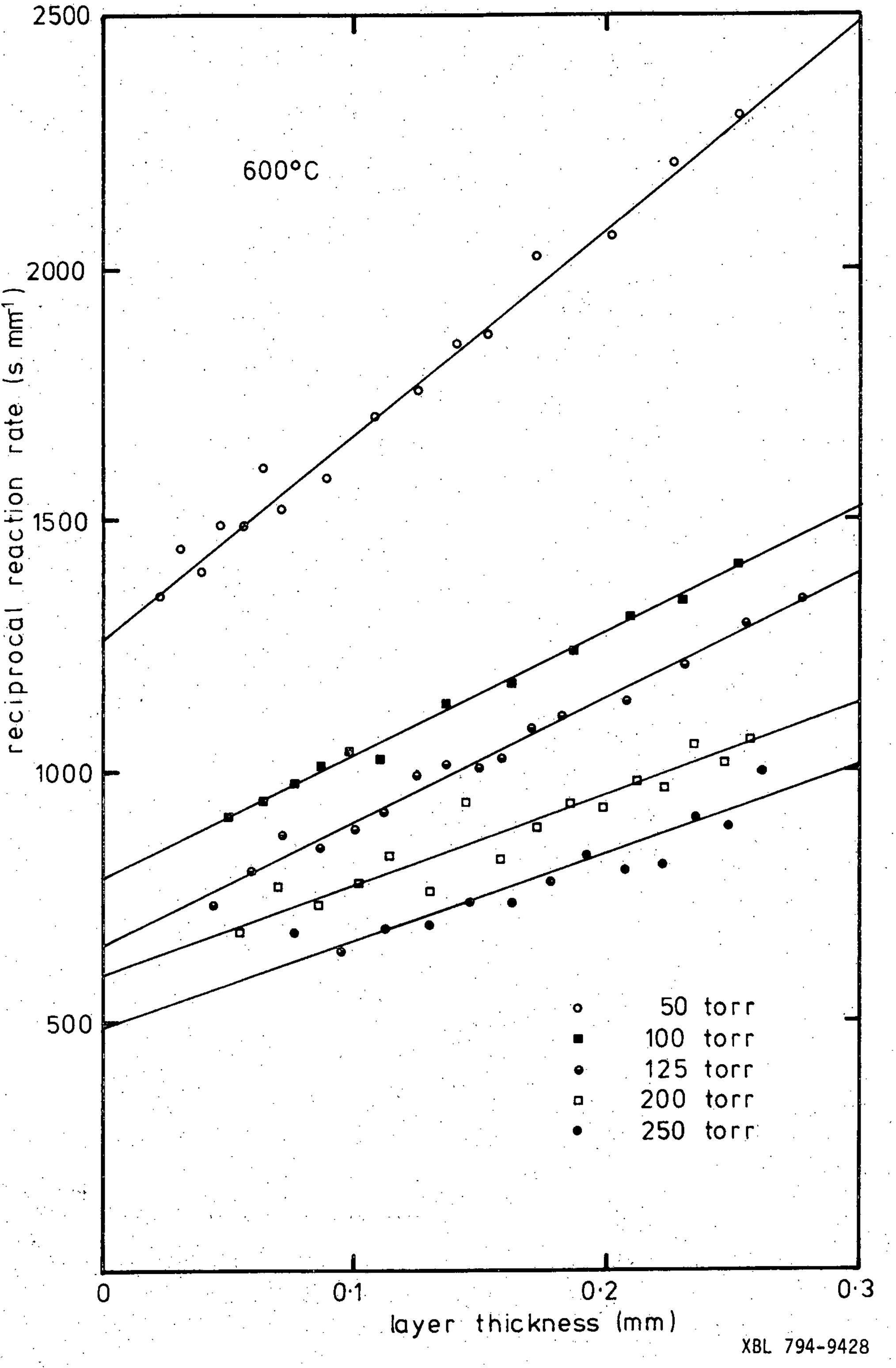
2500
2000
1500
1000
500
0
0·1
0·2
0·3
reciprocal reaction rate (s mm^{-1})
layer thickness (mm)
600°C
○ 50 torr
■ 100 torr
◉ 125 torr
□ 200 torr
● 250 torr
XBL 794-9428

Figure 4 (b)

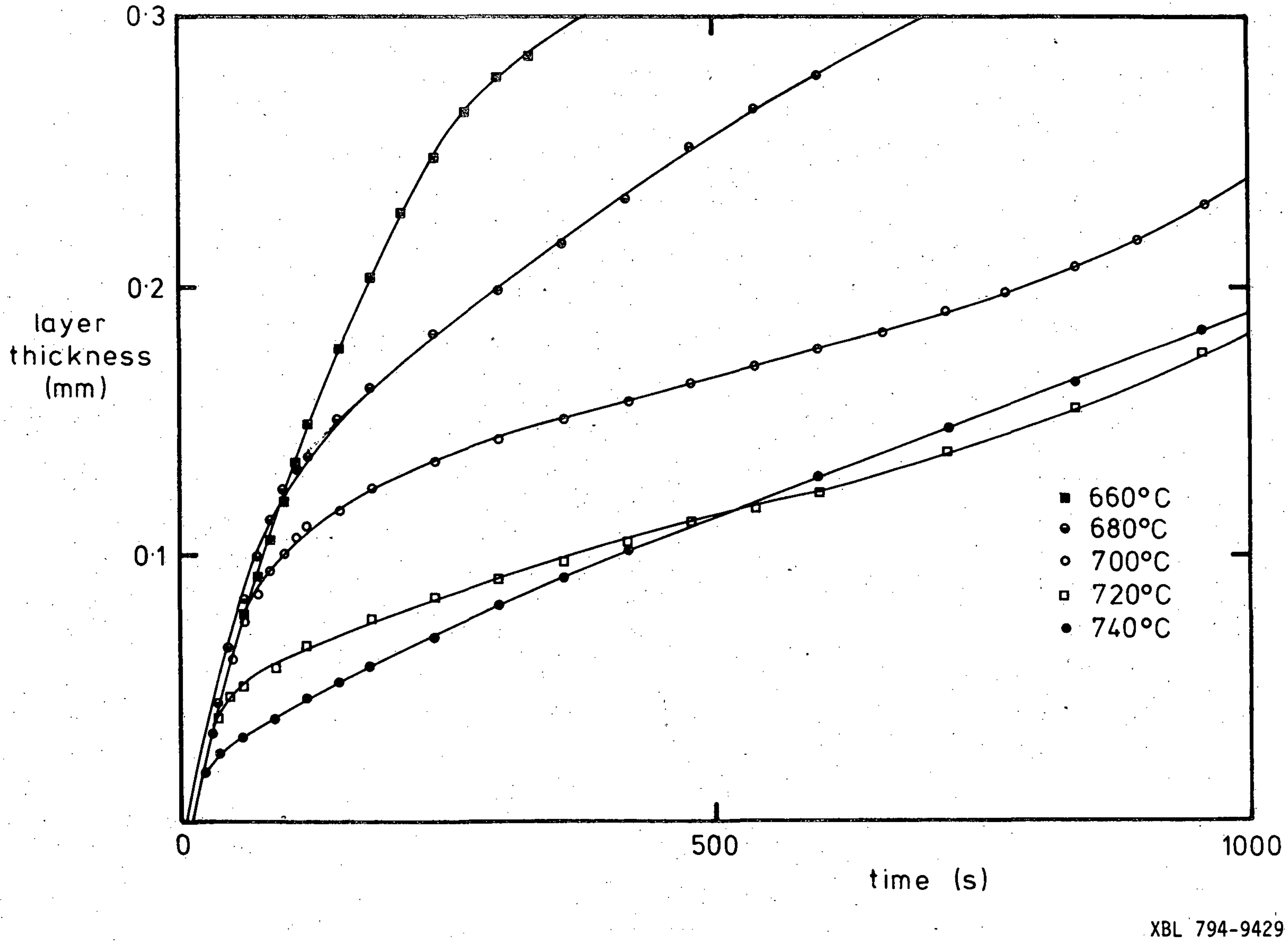
0·3
0·2
0·1
layer thickness (mm)
0
500
1000
time (s)
■ 660°C
◉ 680°C
○ 700°C
□ 720°C
● 740°C
XBL 794-9429

Figure 5

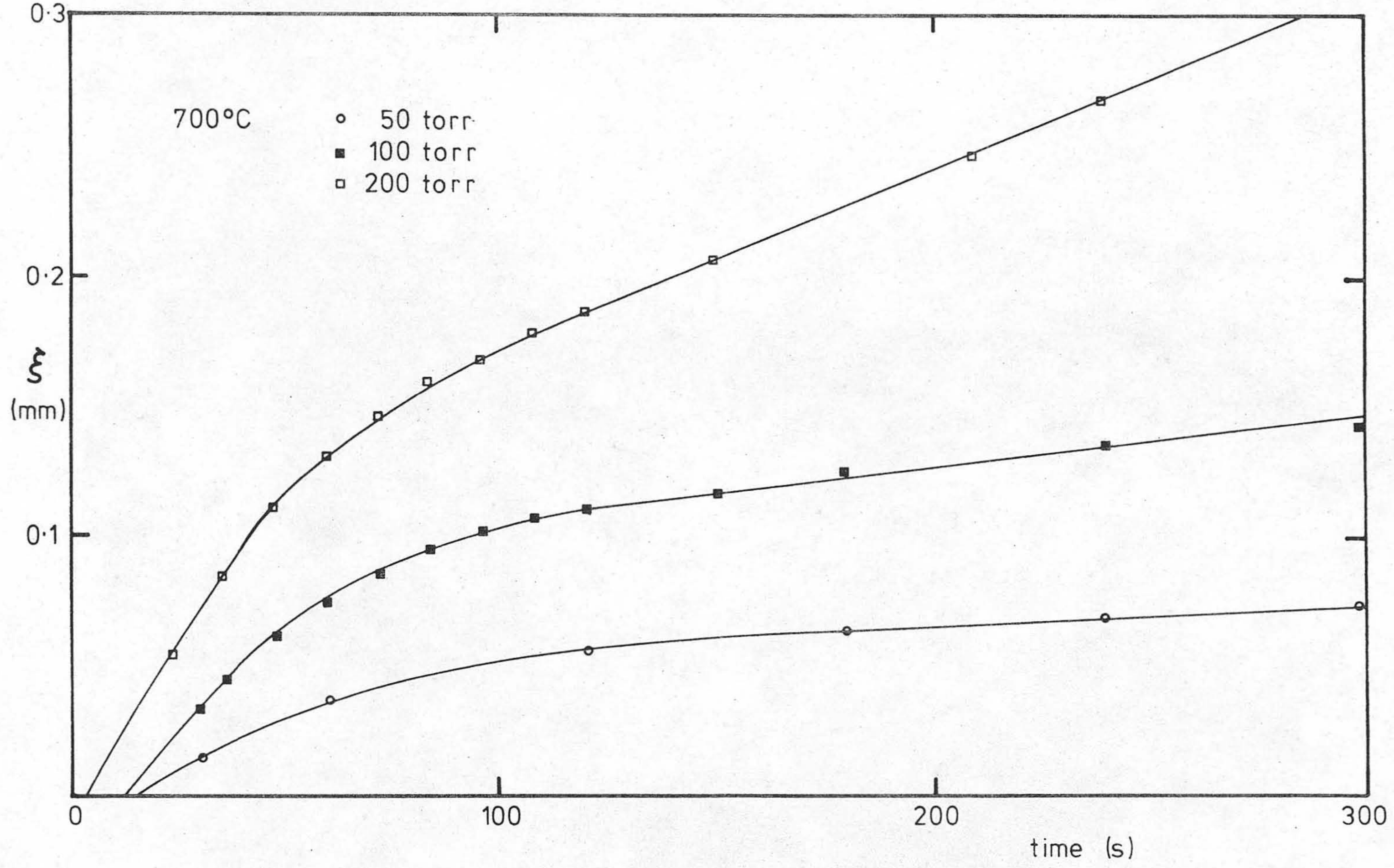

XBL 794-9426

Figure 6

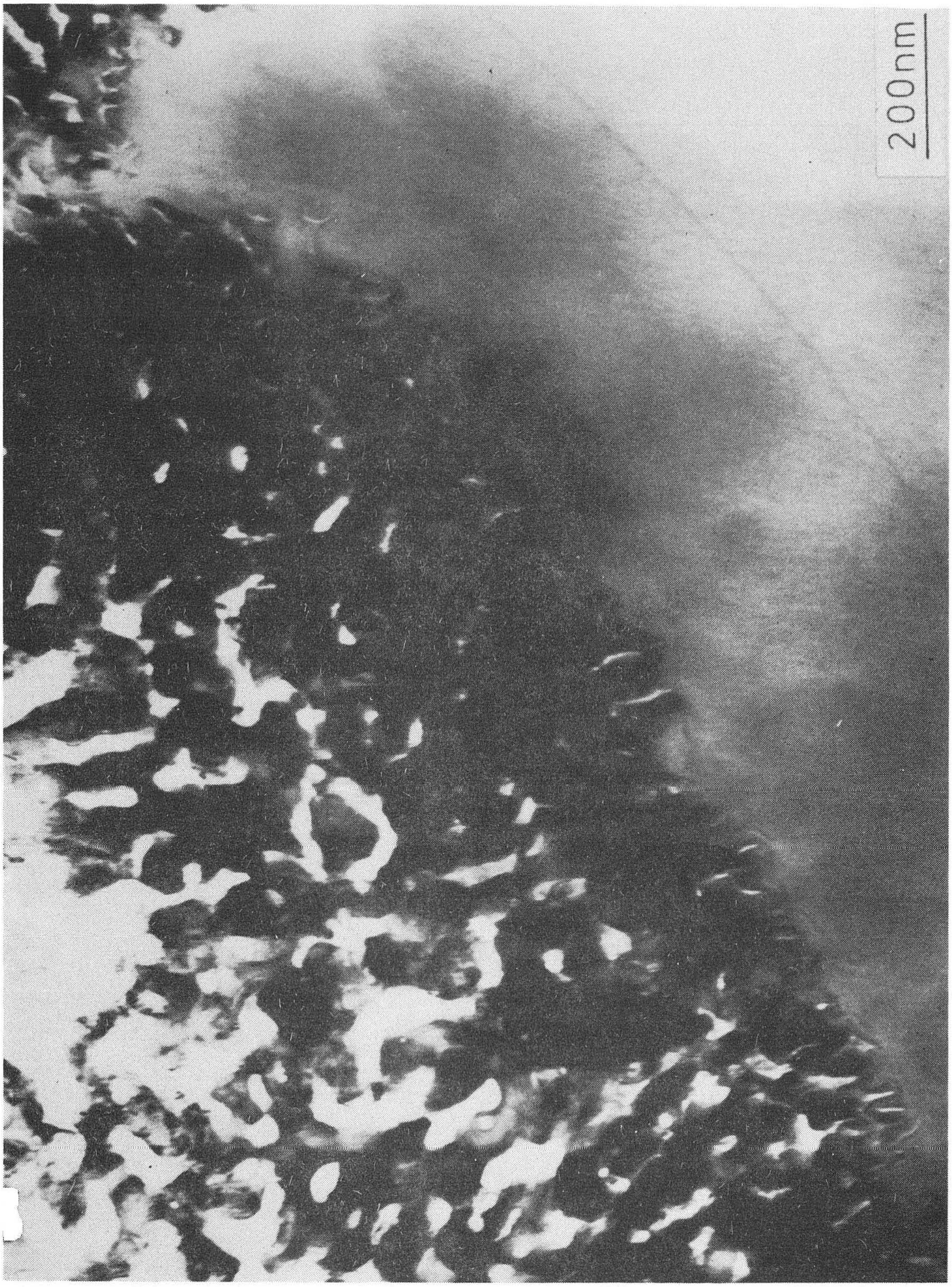

Figure 7

XBB 794-5196

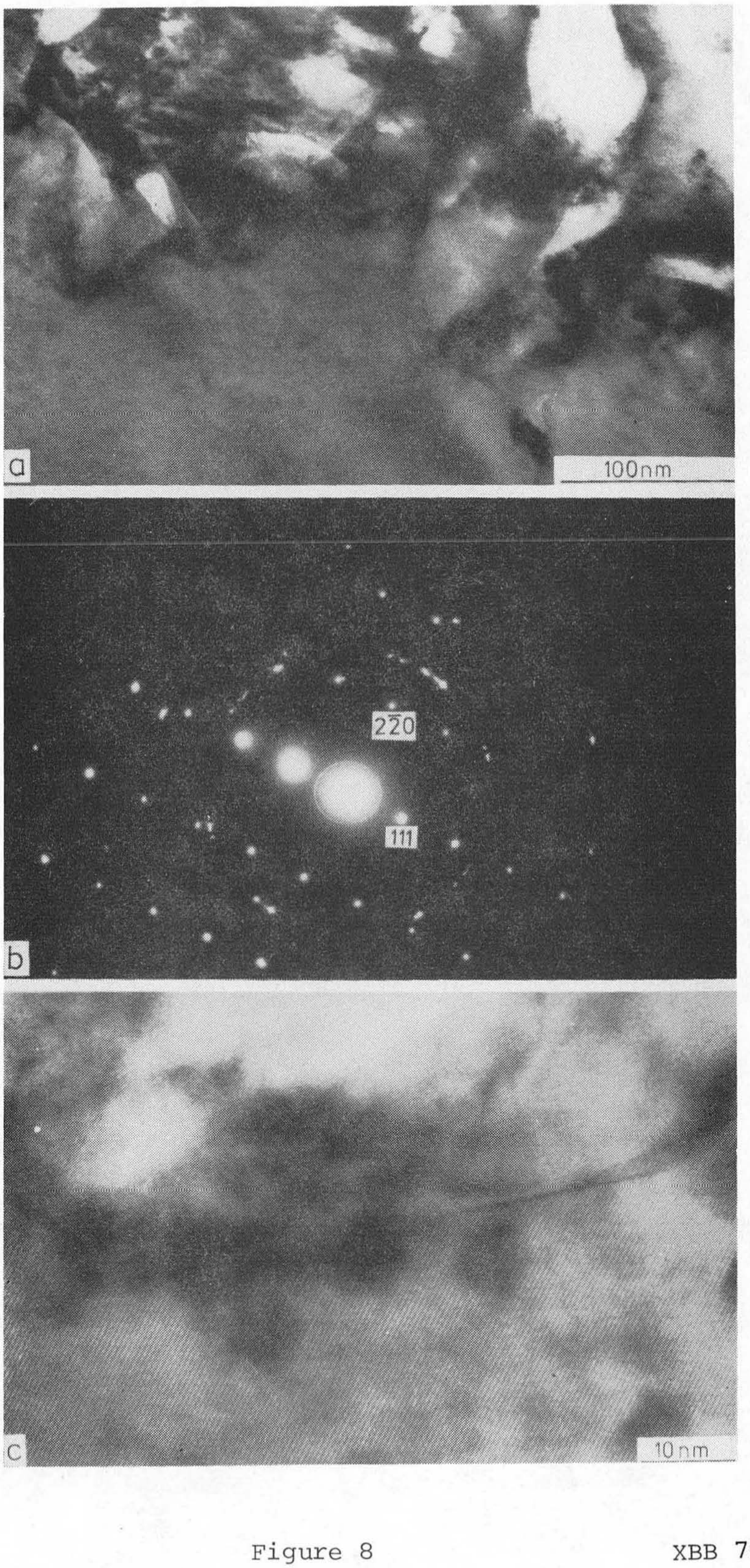

Figure 8

XBB 796-7766

Figure 9

XBB 794-5195

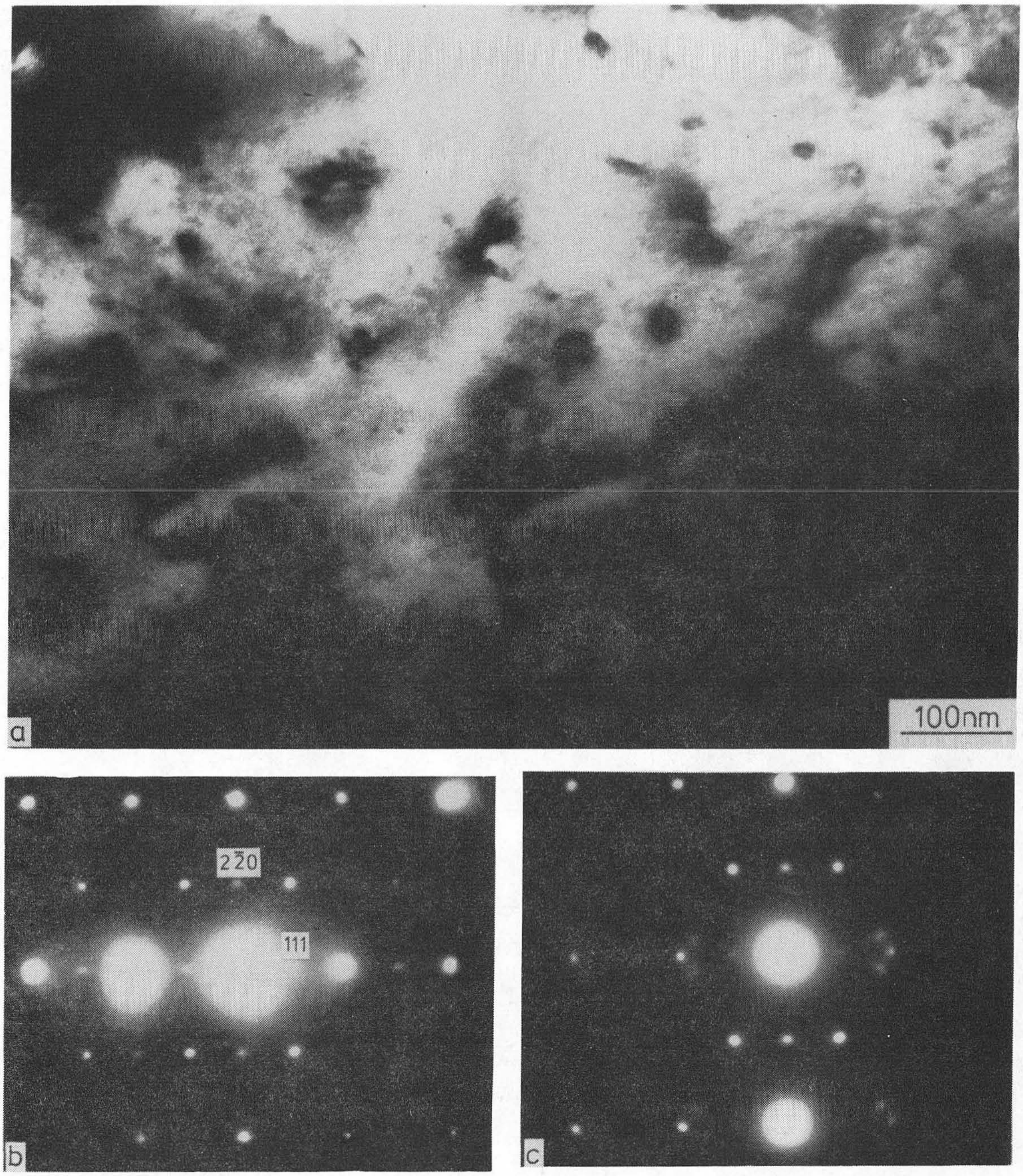

Figure 10

XBB 796-7768

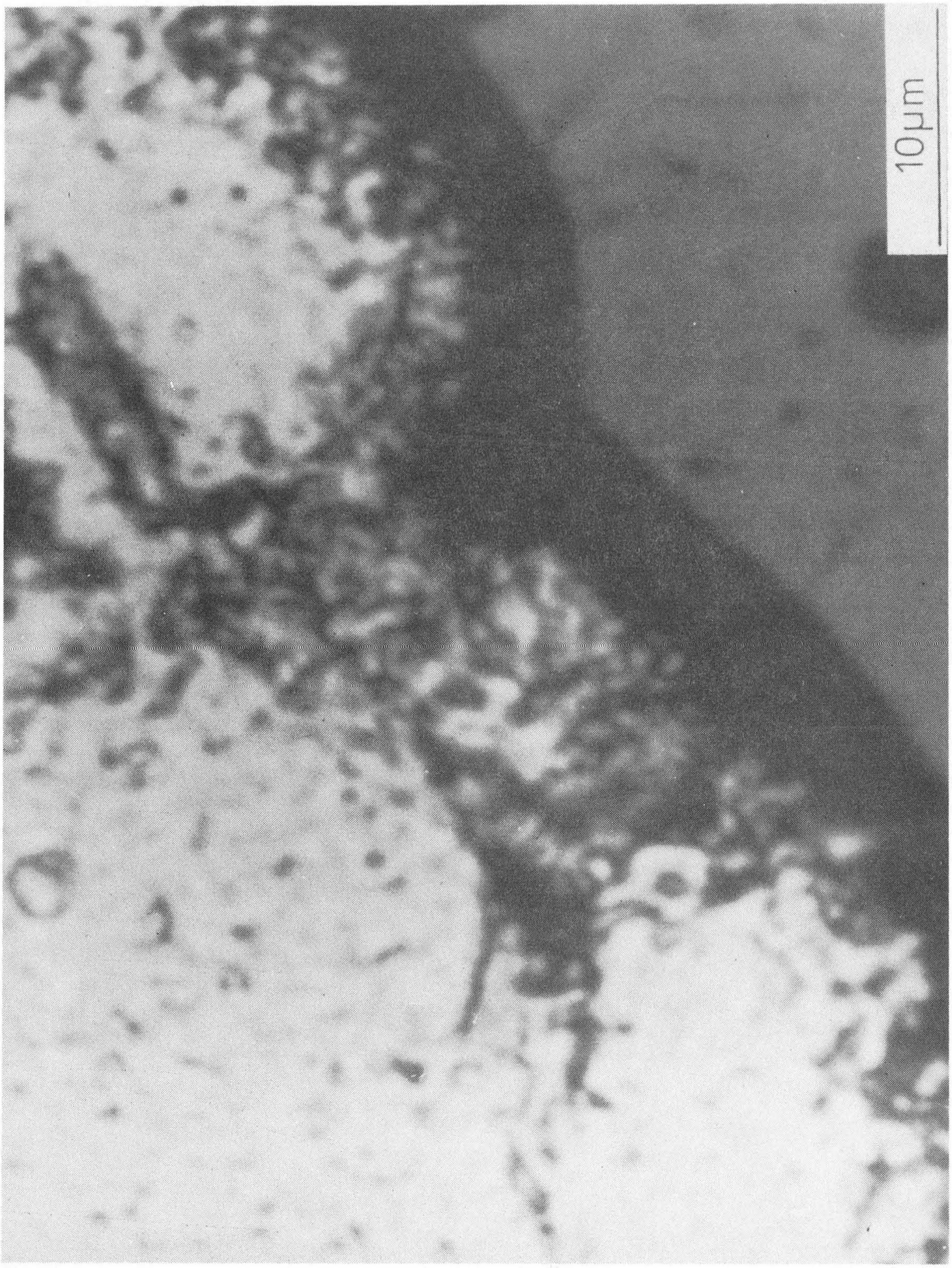

Figure 11

XBB 796-7767

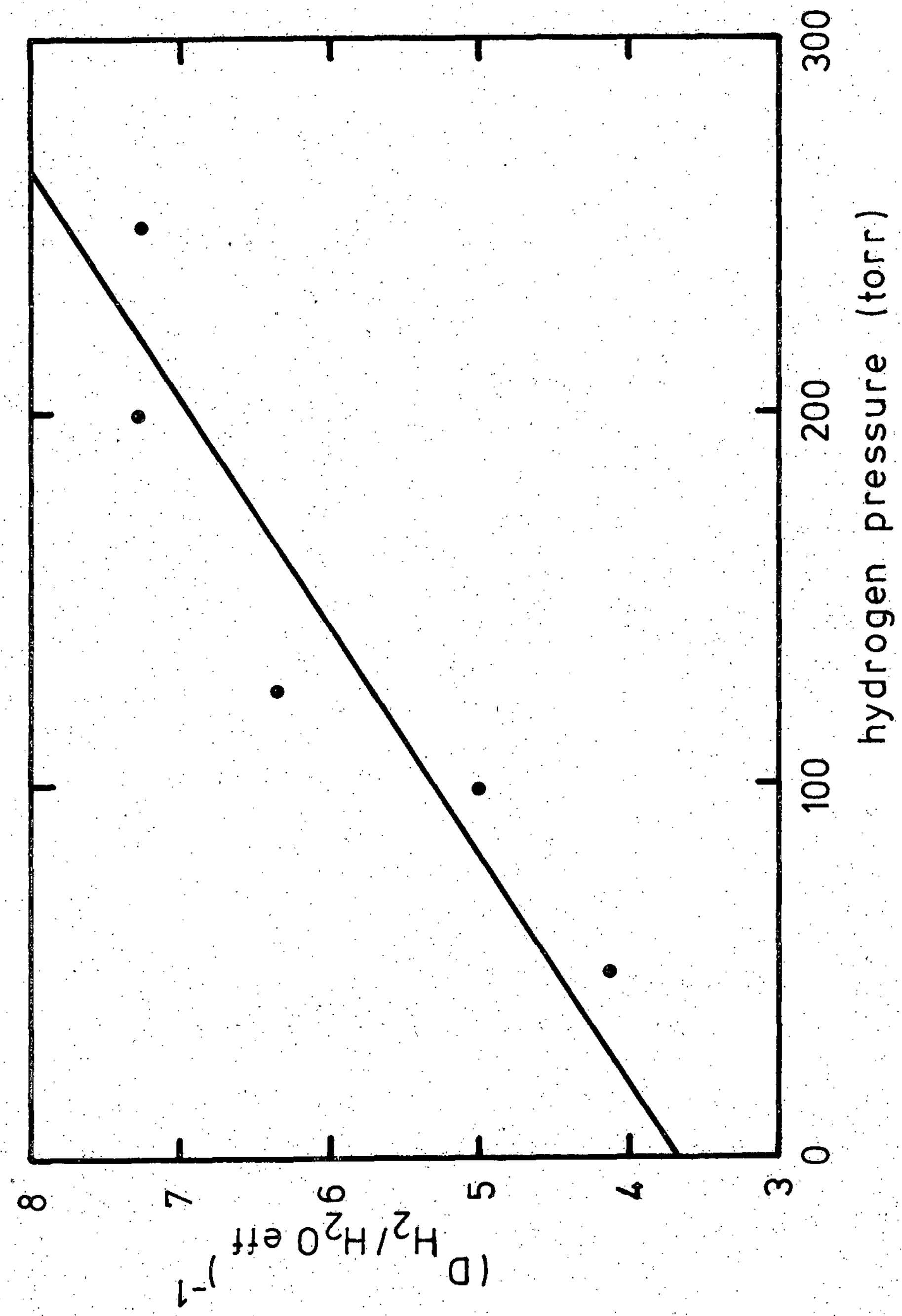

XBL 796-10121

Figure 12

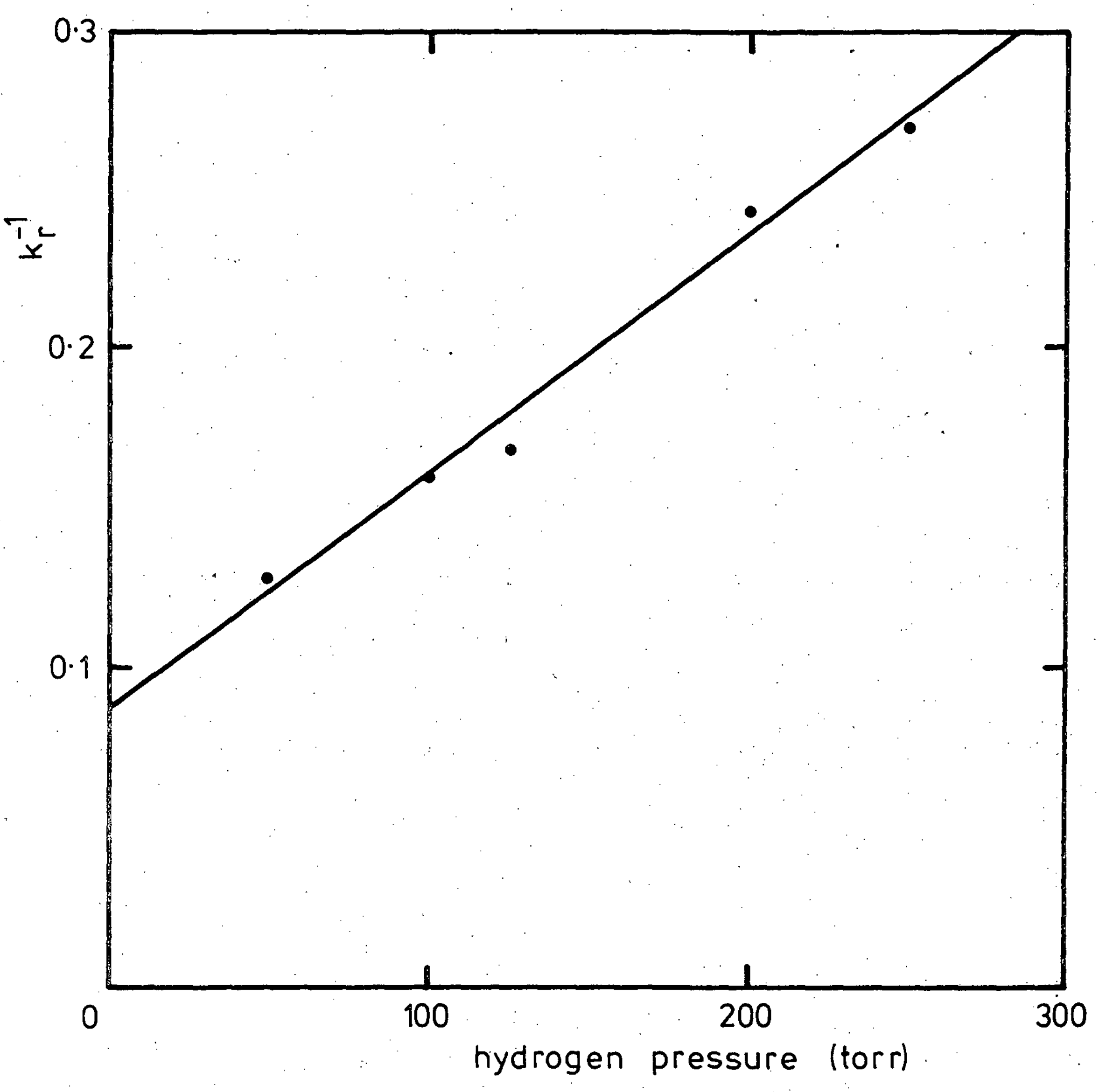

XBL 796-10122

Figure 13

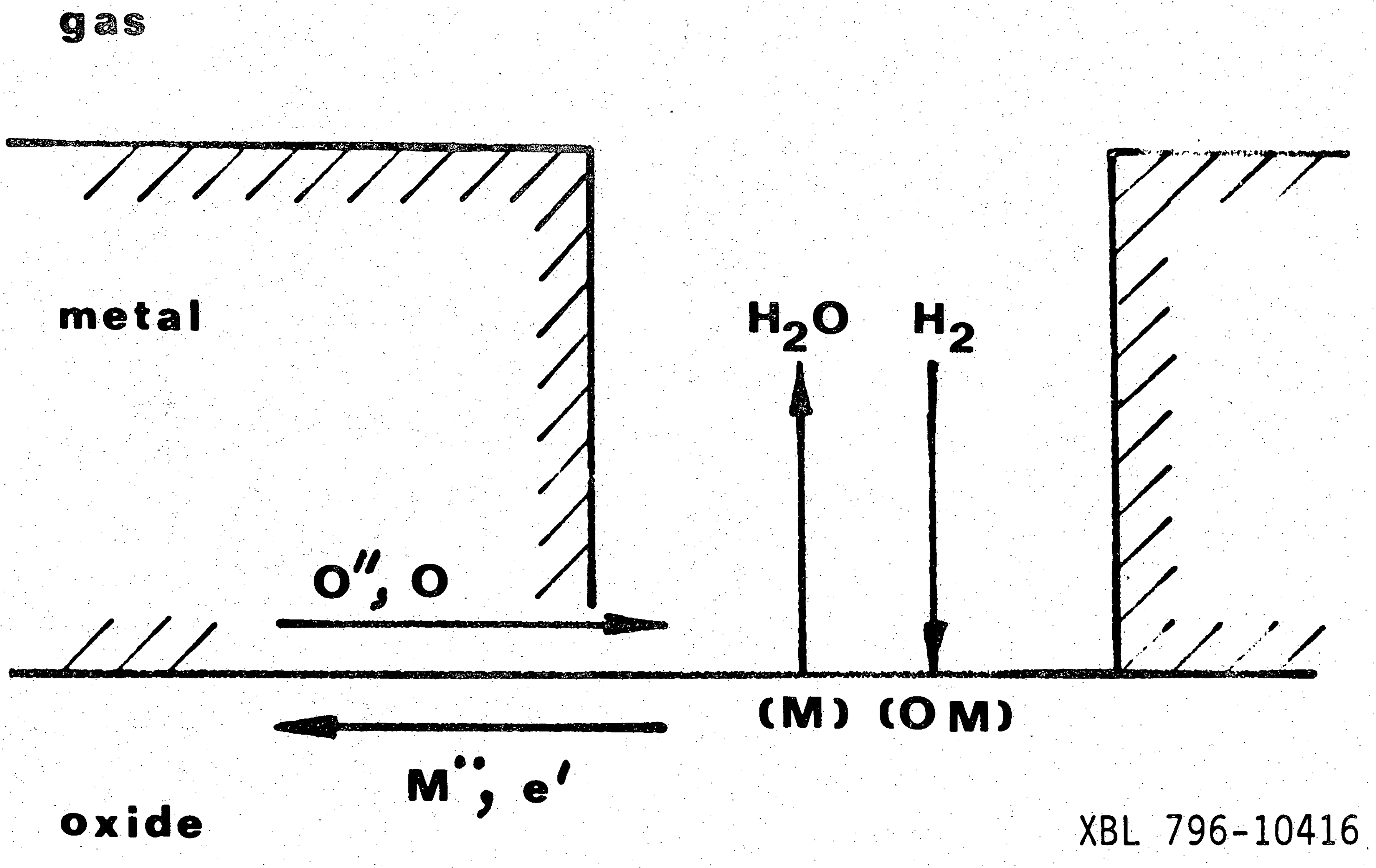

Figure 14

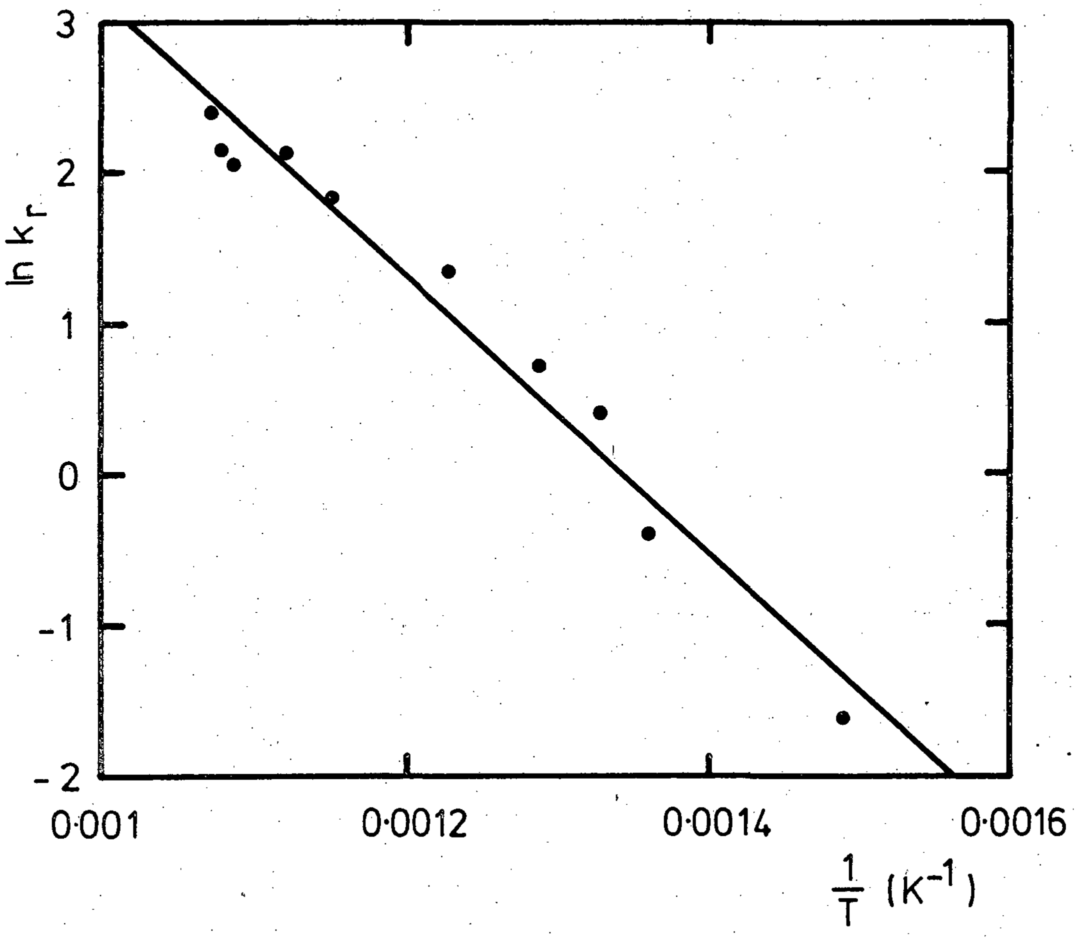

XBL 796-10123

Figure 15

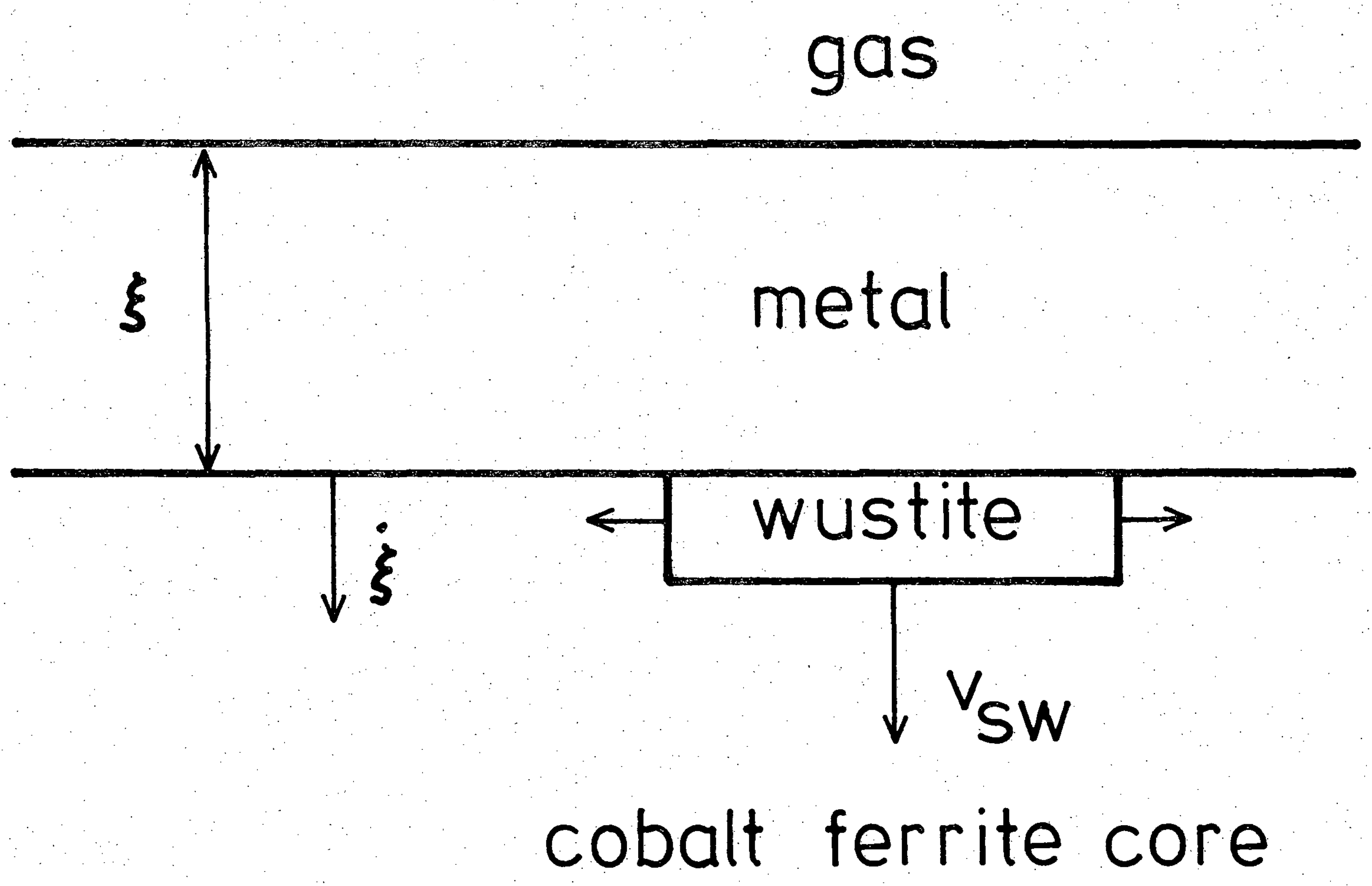

XBL 797-10735

Figure 16

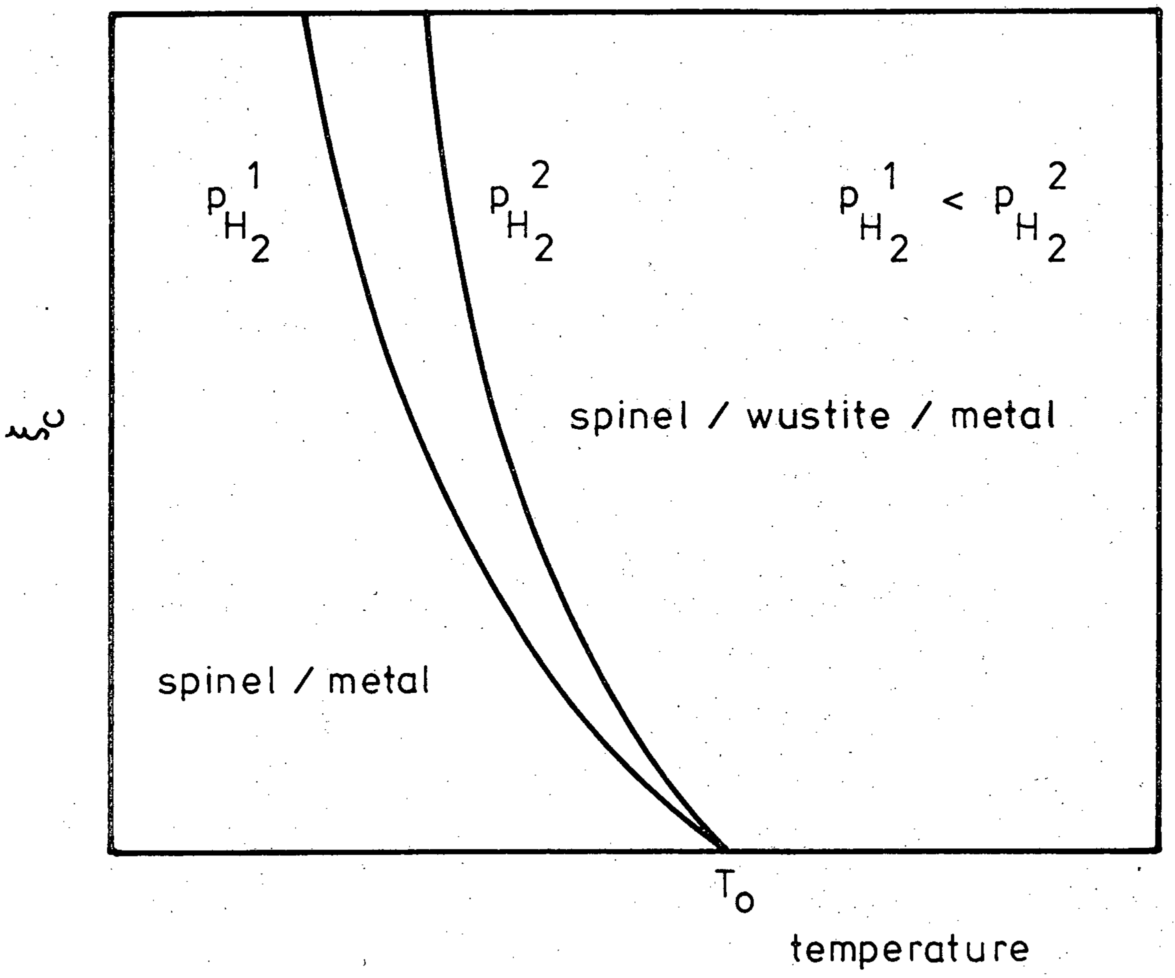

XBL 798-11035

Figure 17

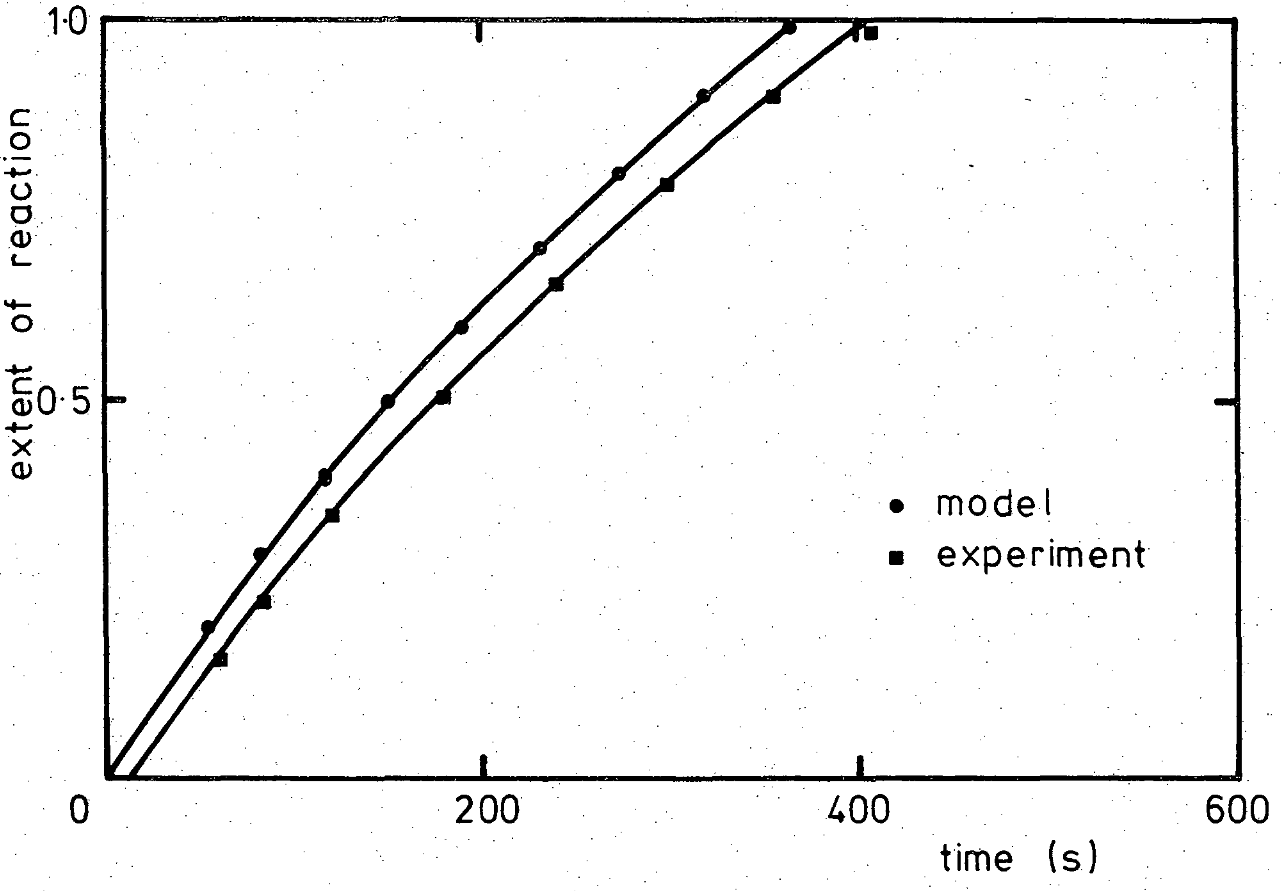

XBL 796-10124

Figure 18

TECHNICAL INFORMATION DEPARTMENT
LAWRENCE BERKELEY LABORATORY
UNIVERSITY OF CALIFORNIA
BERKELEY, CALIFORNIA 94720